

NUMERICAL STUDIES OF
MHD TURBULENCE
IN THE REVERSED FIELD PINCH

David Merlin* and Dieter Biskamp

IPP 6/276

August 1988

*Permanent address: Istituto Gas Ionizzati del CNR, Padova, Italy

Abstract

Nonlinear numerical studies of the MHD turbulence generated in an RFP configuration are presented. In these computations the resistive MHD equations are solved by using a three-dimensional semi-implicit spectral code. While a qualitative picture of the global RFP behaviour is readily obtained, the possibility of obtaining reliable results for Reynolds numbers of practical interest is a major problem. For this reason particular attention is placed on the convergence properties of the spectral methods. Furthermore, preliminary results on the dependence of the fluctuations on the Reynolds numbers are given.

1. Introduction

The reversed field pinch (RFP) is an axisymmetric magnetic configuration in which the toroidal and poloidal magnetic fields are of the same order and the toroidal field at the boundary reverses its direction relatively to the field on axis. The safety factor is less than 1 everywhere in the plasma and becomes negative in the outer region. The main feature of the RFP is that this magnetic configuration is able to maintain itself for times much longer than the resistive diffusion time.

The formation and sustainment of an RFP discharge have been under close theoretical scrutiny, both analytical and numerical, for many years, starting from the historic paper of Taylor /1/, but a complete elucidation of these phenomena is still missing. Taylor's theory shows that a dissipative system, subject to the constraints of constant magnetic helicity and constant toroidal flux, can relax to a minimum energy state, the field being described by the Bessel function model. But this theory does not explain the mechanism by which the reversed state is maintained. The mechanism responsible for this sustainment is generally referred to as the dynamo effect /2,3/.

On the other hand, it now appears quite clear from an increasing number of theoretical papers that this mechanism is closely related to the turbulent nature of the RFP. Present RFP experiments are characterized by magnetic Reynolds numbers of 10^4 to 10^5 and a magnetic fluctuation level of 1% for typical currents of a few hundred kA. The confinement times are shorter and in general the transport properties are even more anomalous than in a tokamak with the same parameters, while the plasma beta is typically higher.

Since new RFP experiments in the MA current range and with magnetic Reynolds numbers of 10^6 to 10^7 are under development /4/, it is very important to obtain a clear understanding of the dynamo effect, its behaviour at high Reynolds numbers, and its relation to transport.

In this respect, numerical solution of the resistive MHD equations represents an important tool in the study of the RFP configuration. In fact, significant numerical work has been done since the early eighties /5,6,7/ in order to clarify the strong relation in the RFP between plasma instabilities and the dynamo mechanism. Present-day supercomputers allow one to solve the primitive set of resistive MHD equations, and in particular three-dimensional simulations of the long-time behaviour of RFP dynamics are now possible.

The present work aims primarily at understanding the limits, in terms of Reynolds

numbers, on full simulation of the MHD equations that are imposed by computer limitations. Attention is also focused on analysis of the turbulent magnetic and kinetic energies for different values of the Reynolds number. In particular, preliminary results on the scaling of the magnetic fluctuations are obtained. In Section 2 the physical model is presented, in Section 3 the numerical algorithm is illustrated, Section 4 shows the results, and some conclusions are drawn in Section 5.

2. The Physical Model

This work is based on numerical solution of the resistive MHD equations. These equations can be written, in dimensionless form, as

$$\frac{\partial \vec{B}}{\partial t} = \nabla \times (\vec{v} \times \vec{B}) - \nabla \times (\eta \vec{J}) , \quad (1)$$

$$\frac{\partial \vec{v}}{\partial t} = -\vec{v} \cdot \nabla \vec{v} - \nabla p + \vec{J} \times \vec{B} + \nu \nabla^2 \vec{v} , \quad (2)$$

$$\frac{\partial p}{\partial t} = -\vec{v} \cdot \nabla p - \gamma p \nabla \cdot \vec{v} + \nabla \cdot (\chi \nabla p) , \quad (3)$$

$$\vec{J} = \nabla \times \vec{B} . \quad (4)$$

The equation for the density ρ is not included in the present formulation, since it is assumed to be constant in space and time in accordance with previous convention /8/. In these equations lengths are normalized to the characteristic scale a of the system (since cylindrical geometry is used, a is assumed to be the plasma radius), and magnetic fields, velocities, and times are normalized to the initial toroidal field on axis B_0 , to the Alfvén velocity ($v_A = B_0/\rho^{1/2}$) and the Alfvén time ($\tau_A = a/v_A$), respectively. Three dissipative effects are considered: an electric resistivity η , a kinetic viscosity ν and a thermal conductivity χ , all defined as scalar quantities with a possible dependence on the minor radius.

These equations describe various phenomena, such as ideal and resistive instabilities as well as resistive, viscous, and thermal diffusion, characterized by highly different spatial and time scales when R^M and R^K are large. Here R^M and R^K indicate the magnetic and kinetic Reynolds numbers, respectively, defined as $R^M = v_A a / \eta$ and $R^K = v_A a / \nu$. The normalization introduced yields $R^M = \eta^{-1}$ and $R^K = \nu^{-1}$.

In this work a zero-pressure plasma is assumed and therefore the results obtained are strictly valid only in the zero beta limit. Since it is known /4/ that RFP configu-

rations are nearly force-free, $J_{\perp}/J_{\parallel} \approx \beta \approx 0.1$, this approximation can be considered to be adequate.

3. The Numerical Algorithm

3.1. The Spectral Formulation

The system of equations (1,2,4) is solved in cylindrical coordinates (r, θ, z) . The plasma is considered to be in contact with a conducting wall. Since the lengths are normalized to the plasma minor radius, the domain of integration is $0 \leq r \leq 1$, $0 \leq \theta \leq 2\pi$, and $0 \leq z \leq 2\pi R$, where R is the major radius of the rectified torus. The spatial discretization of the various quantities and operators is assumed to be of the finite-difference type in the radial direction and spectral in the poloidal and axial directions. Two staggered uniform radial meshes of N_r points are used, together with N_{θ} poloidal and N_z axial Fourier components. In this approximation any physical quantity is written as a finite Fourier series:

$$f(r_i, \theta, z; t) = \sum_{m=-N_{\theta}/2}^{N_{\theta}/2-1} \sum_{n=-N_z/2}^{N_z/2-1} f_{m,n}(r_i; t) \exp \left[i \left(m\theta + \frac{n}{R} z \right) \right]. \quad (5)$$

The discrete Fourier transform $f_{m,n}$ of f is given by the complex coefficients:

$$f_{m,n}(r_i; t) = \frac{1}{N_{\theta} N_z} \sum_{j=0}^{N_{\theta}-1} \sum_{k=0}^{N_z-1} f(r_i, \theta_j, z_k; t) \exp \left[-i \left(m\theta_j + \frac{n}{R} z_k \right) \right], \quad (6)$$

where

$$\theta_j = 2\pi j / N_{\theta} \quad j = 0, \dots, N_{\theta} - 1$$

$$z_k = 2\pi R k / N_z \quad k = 0, \dots, N_z - 1$$

are the collocation points of the spectral expansion /9/. The imposition of the reality of $f(r, \theta, z; t)$ implies

$$f_{-m, -n} = f_{m, n}^*. \quad (7)$$

Inserting eq. (5) into eqs. (1,2,4) yields a system of $N_{\theta} \times N_z$ sets of equations like

$$\frac{\partial \vec{B}_{m,n}}{\partial t} = [\nabla \times (\vec{v} \times \vec{B})]_{m,n} - [\nabla \times (\eta \vec{J})]_{m,n}, \quad (8)$$

$$\frac{\partial \vec{v}_{m,n}}{\partial t} = -[\vec{v} \cdot \nabla \vec{v}]_{m,n} + [\vec{J} \times \vec{B}]_{m,n} + [\nu \nabla^2 \vec{v}]_{m,n} , \quad (9)$$

$$\vec{J}_{m,n} = [\nabla \times \vec{B}]_{m,n} , \quad (10)$$

where $[\]_{m,n}$ denotes the (m,n) Fourier component of the term inside the brackets. As is clear, these equations are defined in the Fourier space: they represent the spectral formulation of the problem.

The convolution sums of the nonlinear terms are computed through a pseudospectral algorithm /9/. Fast Fourier transforms are used to communicate between the configuration (real) space and the Fourier space. The pseudospectral formulation involves the inconvenience of aliasing errors generated by the nonlinearities. The most practical way to eliminate such errors, as adopted here, is to use only 2/3 of the available Fourier space for each dimension, discarding the highest-mode-number part of the spectrum of all field quantities. In the present case this corresponds to the use of only 4/9 of the two-dimensional Fourier space.

3.2. Time Advance and Semi-implicit Term

When numerically solving eqs. (1,2,4) for the RFP, one is generally interested in the long-time behaviour, which is characterized by the appearance of relaxation and dynamo phenomena. But numerical stability restrictions on the time step for the standard explicit schemes or, on the other hand, the fundamental problems arising from the nonlinear terms using implicit schemes would make any study of long-time, low-frequency phenomena very difficult and expensive, even with the most advanced supercomputers.

Recently, the situation has been improved by introducing in plasma physics /8,10,11/ the semi-implicit method currently used in numerical weather predictions /12/. The main feature of this algorithm is that it eliminates the most severe time step restrictions associated with the fastest modes of the system (compressional and shear Alfvén) while essentially retaining the simplicity and flexibility of an explicit scheme.

To advance the equations in time, the following scheme is adopted (the mode number indices are omitted):

$$\frac{\vec{B}^* - \vec{B}^n}{\Delta t/2} = \nabla \times (\vec{v}^n \times \vec{B}^n) , \quad (11)$$

$$\vec{J}^* = \nabla \times \vec{B}^* , \quad (12)$$

$$\frac{\vec{v}^{n+1} - \vec{v}^n}{\Delta t} = -\vec{v}^n \cdot \nabla \vec{v}^n - \vec{B}^* \times \vec{J}^* + \nu \nabla^2 \vec{v}^{n+1}, \quad (13)$$

$$\frac{\vec{B}^{n+1} - \vec{B}^n}{\Delta t} = \nabla \times \left(\frac{\vec{v}^{n+1} + \vec{v}^n}{2} \times \vec{B}^* \right) - \nabla \times (\eta \nabla \times \vec{B}^{n+1}). \quad (14)$$

Equations (11,12) correspond to a predictor step (but without taking into account the dissipative terms) to evaluate the magnetic field and the current density at the time $t^n + \Delta t/2$. These values are then used in eq. (13) to advance the velocity to the time t^{n+1} . Note in this equation that the advective term $\vec{v} \cdot \nabla \vec{v}$ is evaluated at the time t^n . Once the new velocity is known, eq. (14) is used to calculate \vec{B} at the time t^{n+1} . In eqs. (13,14) the dissipative terms are implicit.

The algorithm described by eqs. (11-14) is linearly stable only if the Courant-Friedrichs-Lewy condition on the time step is satisfied. In particular, the most severe time step restrictions are imposed by fast compressional and shear Alfvén modes.

The semi-implicit method eliminates these restrictions, so that the time step is no longer determined by stability constraints but rather by numerical accuracy. The method amounts to adding new terms in the equations that do not affect the solution as $\Delta t \rightarrow 0$ and make the algorithm unconditionally linearly stable (time step limitations may occasionally arise owing to the nonlinear terms). In particular, for the present case, it has proved /8/ particularly convenient to modify the momentum equation (2) by adding a linear term

$$\frac{\partial \vec{v}}{\partial t} = \vec{F} + \alpha \Delta t \nabla^2 \frac{\partial \vec{v}}{\partial t}, \quad (15)$$

where \vec{F} represents the right-hand side of eq. (2) and α is a numerical constant. Discretizing eq. (15),

$$\frac{\vec{v}^{n+1} - \vec{v}^n}{\Delta t} = \vec{F} + \alpha \nabla^2 (\vec{v}^{n+1} - \vec{v}^n),$$

it is clear that the semi-implicit term can be considered as a sort of artificial viscosity. In this case, in which the viscosity term is implicit, this semi-implicit operator can very easily be implemented. From eq. (15) note also that in the limit $\partial \vec{v} / \partial t \rightarrow 0$ the original system is unaffected: this means that steady-state solutions are solutions of the original equations.

3.3. Boundary Conditions

At the origin $r = 0$ analytic conditions based on regularity and single-valuedness considerations must be imposed for the various m . In particular, for \vec{B} and \vec{v} the

following conditions are applied at $r = 0$ (' denotes the radial derivative):

$$\begin{array}{llll}
m = 0 & m \neq 0 & |m| = 1 & |m| \neq 1 \\
B_z' = 0 & B_z = 0 & B_r' = 0 & B_r = 0 \\
v_z' = 0 & v_z = 0 & B_\theta = imB_r & B_\theta = 0 \\
& & v_r' = 0 & v_r = 0 \\
& & v_\theta = imv_r & v_\theta = 0
\end{array}$$

The plasma is assumed to be surrounded by a conducting wall, with no vacuum region between the plasma and the wall. This wall is assumed to be perfectly conducting for all but the (0,0) mode. For this mode constant axial current (i.e. $B_\theta(1) = \text{const.}$) and constant axial flux ($\Phi_z = \text{const.}$) or, alternatively, constant axial field ($B_z(1) = \text{const.}$) boundary conditions are applied. Furthermore, owing to the presence of the viscosity, one is free to specify the boundary conditions for the poloidal and axial components of the velocity. To summarize, the following conditions are applied at $r = 1$:

$$\begin{array}{llll}
\text{all} & \text{modes} & (m,n) = (0,0) & (m,n) \neq (0,0) \\
B_r = 0 & & B_\theta = \text{const.} & (rB_\theta)' = 0 \\
v_r = 0 & & \Phi_z = \text{const.} \text{ or} & B_z' = 0 \\
v_\theta = 0 & & B_z = \text{const.} & \\
v_z = 0 & & &
\end{array}$$

4. Applications

To characterize the RFP configuration, it is useful to introduce two quantities referring to the mean field ((0,0) mode):

the pinch parameter

$$\Theta = \frac{B_\theta(1)}{\langle B_z \rangle},$$

and the field reversal parameter

$$F = \frac{B_z(1)}{\langle B_z \rangle},$$

where $\langle B_z \rangle$ is the average of the axial field over the plasma cross-section.

As stated in the previous section, the boundary condition adopted here for the mean poloidal magnetic field is $B_\theta(1) = \text{const.}$, corresponding to the constancy of the total toroidal current. Furthermore, for the axial component of the mean magnetic field, the condition of vanishing derivative at the boundary is chosen, which can easily be seen to correspond to the conservation of the axial flux, i.e. of $\langle B_z \rangle$. Therefore Θ must remain constant in time, while in general F will show a temporal dependence.

These boundary conditions for the mean field make the system strongly driven from the outside since there is continuous input of electromagnetic energy. In fact, the Poynting vector at $r = 1$ can be written as

$$\vec{E} \times \vec{B} = -\hat{r} E_z B_\theta = -\hat{r} \eta \frac{B_\theta}{r} \frac{\partial}{\partial r} (r B_\theta). \quad (16)$$

It is generally said that the dynamo action is “demonstrated”, under these or similar boundary conditions, if the reversal of the axial field ($F < 0$) is maintained. This cannot be obtained in a purely axisymmetric way but requires the presence of modes $(m, n) \neq (0, 0)$ in the spectrum. An example of the temporal evolution keeping only the mean field is shown in Fig. 1: the initial state, which is slightly reversed, is immediately lost and eventually a steady state, not reversed, is produced by the action of inward convection and diffusion.

4.1. Results for Low Reynolds Numbers

The resistivity profiles used in this work are flat in the central region and sharply increasing at the outer boundary, according to the simple analytic expression

$$\eta(r) = \eta(0) [1 + (\alpha - 1)r^\beta].$$

Here α directly gives the value of the resistivity at the outer boundary with respect to the on-axis value. Typical values for α and β are 20 and 10, respectively.

The code is first applied to a case previously studied /8/. The initial-equilibrium magnetic profiles are described by the safety factor:

$$q(r) = 0.4(1 - 1.8748r^2 + 0.83232r^4)$$

with an aspect ratio of 1. The value of the pinch parameter associated with this q profile is $\Theta = 1.7$, which will be maintained in time. This equilibrium, which

is strongly unstable with respect to the $(m = 1, n = -2)$ mode, is perturbed by introducing the linear eigenfunctions of the $(m = 1, n = -1)$ and $(m = 1, n = -2)$ modes, at an amplitude of 10^{-5} with respect to the mean field. The on-axis resistivity is set at 10^{-3} , while for the viscosity a value of 10^{-4} is chosen. The magnetic and kinetic Reynolds numbers therefore assume the values 10^3 and 10^4 , respectively. The numerical resolution is given by $N_r = 100$ radial points, $N_\theta = 8$ poloidal modes, and $N_z = 16$ axial modes. The evolution from the initial state is computed for 500 Alfvén times.

In Fig. 2 the time evolution of the term $E_z B_\theta$ of eq. (16) is shown. As can be seen, the boundary conditions used imply the presence of a non-vanishing axial electric field E_z at the wall. In Fig. 3 the temporal behaviour of the field reversal parameter F is shown: initially the configuration loses the reversal immediately but, owing to the action of the unstable modes, it is regained after $\sim 50\tau_A$ and maintained at a quasi-steady level. The dynamics of this process can be illustrated by the evolution of the magnetic energy of the individual modes:

$$E_{m,n}^M = \frac{1}{2} \int |\vec{B}_{m,n}|^2 d^3x. \quad (17)$$

In Fig. 4a the magnetic energy of the modes characterized by a negative value of n is shown. These modes can only be resonant between the axis and the reversal surface. Hence they are often called internal. Analogously, the energies of the other modes are shown in Figs. 4b,c. Modes with positive n value, also called external, can only be resonant between the reversal and the outer boundary, while the $m = 0$ are always resonant on the reversal surface. From these figures it is clear that the internal modes play the key role in the phenomenon under examination, their energies being substantially greater than those of the other modes. The external modes, at least in this case with a perfectly conducting wall, do not play any significant role, while the $m = 0$ modes are directly excited by the nonlinear coupling of the $m = 1$ modes.

In Fig. 4a, the initial phase following the initial rapid loss of the field reversal is dominated by the exponential growth of the unstable mode $(1, -2)$ and its harmonic $(2, -4)$. The interaction of these modes with the mean field is such that the mean toroidal field reverses and the modes saturate, giving rise to a stationary phase, between $t \sim 50$ and $t \sim 200$, dominated by a single helicity. But this state turns out to be unstable with respect to the $(1, -3)$ mode, which in fact grows exponentially. At $t \sim 200$ the two modes $(1, -2)$ and $(1, -3)$ interact, giving rise to a quasi-stationary state characterized by the presence of these two dominant modes and a field reversal ratio $F \sim 0.03$. This result is quite similar to that obtained in [8], a steady

state finally dominated by $(1, -2)$ and $(1, -4)$ modes, but differences in the boundary conditions and in the diffusion coefficients may account for the difference.

An aspect ratio of 1, as considered in the previous case, is of course unrealistic. Typical values of the aspect ratio for the RFP configuration are 4 to 5. On the other hand, working with such high values of R/a implies the necessity to use a correspondingly larger axial wave number spectrum since the characteristic axial wave numbers for the dominant $m = 1$ modes are proportional to R/a : the $(1, -2)$ mode for $R/a = 1$ is transposed into the $(1, -10)$ mode for $R/a = 5$. Of course, as the aspect ratio increases, the dynamics can also change since more modes are present. Because of the memory limitations of the computer, an aspect ratio of 2 is adopted as a "compromise" in the rest of this work.

Having an aspect ratio of 2 and including more modes does not basically change the results of the previous case. Using a mesh of $100 \times 8 \times 32$ points, a q on axis of 0.2 instead of 0.4, and an initial perturbation composed of the modes $(m = 1, n = -1, -2, -3, -4)$, each at an amplitude of 10^{-5} , one finds that the results are in agreement with the previous ones. Now the dominant modes are $(1, -4)$ and $(1, -6)$, and they show exactly the same behaviour as the $(1, -2)$ and $(1, -3)$ modes of Fig. 4a.

Decreasing the on-axis resistivity to $3 \cdot 10^{-4}$, while maintaining the viscosity at 10^{-4} , one obtains a more turbulent situation than in the previous case. The resolution, the initial, equilibrium and the initial perturbation are not changed. In Fig. 5 the temporal evolution of the field reversal F is shown. The main temporal variations in F can be connected with the continuous excitation, saturation, and decay of different internal modes. This mechanism appears clear in the evolution of the internal modes, as shown in Fig. 6. In this process an important role is also played by the convection and diffusion of the mean field. At the end of this run, at $t = 500$, the dominant modes are again $(1, -4)$ and $(1, -6)$.

Considering Ohm's law

$$\vec{E} + \vec{v} \times \vec{B} = \eta \vec{J}$$

and taking the poloidal component for the mean field ($_0$ denotes mean quantities, and δ fluctuating quantities, where the average is made over the poloidal and axial directions) one obtains

$$E_{\theta 0} - v_{r0} B_{z0} + \langle \delta \vec{v} \times \delta \vec{B} \rangle_\theta = \eta J_{\theta 0}. \quad (18)$$

Owing to the boundary condition $E_{\theta 0}(1) = 0$, the steady state is characterized by $E_{\theta 0} = 0$ over the whole radius. On the reversal surface the poloidal current cannot

be due to the term $v_{r0}B_{z0}$, which vanishes. The only term which can sustain $J_{\theta0}$ at this point is the nonlinear term due to the fluctuations. These considerations are illustrated in Fig. 7, where the terms of eq. (18) are shown, for the final state of Fig. 5: curves 1, 2, and 3 denote the poloidal voltage $\eta J_{\theta0}$, the $v_{r0}B_{z0}$ term, and the contribution of the fluctuations, respectively, while the dotted line denotes the poloidal electric field. $E_{\theta0}$ is very close to zero throughout the radius, indicating that the whole system has reached a quasi-stationary state. It is clear from Fig. 7 that in general the poloidal current is sustained by both the $v_{r0}B_{z0}$ contribution and the fluctuating term $-\langle \delta \vec{v} \times \delta \vec{B} \rangle_{\theta}$, while at the reversal only the latter contributes. This is the reason why this fluctuating term is often referred to as the dynamo term and the dominant modes in it, typically internal resonant modes, are called dynamo modes.

The final state of Fig. 5 is taken as the initial state in most of the runs which will be subsequently considered, since here attention is focused on analysis of the fully developed turbulent states rather than on situations which are strongly dependent on the initial conditions.

4.2. Convergence Studies

An important characteristic of spectral methods is their self-diagnosing property: insufficient grid resolution manifests itself in excessive values of high-mode-number expansion coefficients. For the present problem a careful analysis of the magnetic and kinetic energy spectra allows one to decide whether or not a particular result can be considered reliable.

In this section attention is focused on a convergence analysis of the solutions obtained by the spectral code, for the case in which the resistivity and the viscosity both have the value $3 \cdot 10^{-4}$. The initial state is that discussed at the end of the previous section. Three cases, characterized by different spectral resolutions, are first considered:

case	$N_r \times N_{\theta} \times N_z$	$m_{max} \times n_{max}$
<i>a</i>	$100 \times 8 \times 64$	2×21
<i>b</i>	$100 \times 12 \times 96$	3×32
<i>c</i>	$100 \times 16 \times 96$	5×32

The third column lists the maximum absolute values of the poloidal and axial mode numbers ($-m_{max} \leq m \leq m_{max}$, $-n_{max} \leq n \leq n_{max}$).

The three cases are computed up to $t = 410$. The typical mean magnetic field profiles, averaged in time, obtained in these runs are given in Fig. 8, which refers to case *c*. In Fig. 9 the behaviour of the field reversal parameter is given: it can be seen how the mean value depends on the mesh. Cases *b* and *c* do not differ from each other in any significant way. Of course, case *c* should be considered as the one closest to the exact solution, but the dynamics of the system is also sufficiently well described in case *b*. In case *a* the spectral resolution is too poor, even at these relatively low Reynolds numbers, to give a reliable solution, and the reversal parameter clearly differs from the other two cases.

The differences observed in the field reversal behaviour are, of course, a consequence of the different behaviour of the modes. In Fig. 10 the time evolutions of the total magnetic and kinetic energies of the perturbation are given. The main part of the perturbed energy is magnetic but the kinetic contribution is non-negligible: roughly speaking, there is an order of magnitude between the two. On average the magnetic energies for cases *b* and *c* are quite similar, while that for case *a* is somewhat lower. On the other hand, the kinetic energy shows the opposite behaviour: it tends to decrease as the number of modes increases and there is also a non-negligible difference between cases *b* and *c*. It should be noted that the difference in the behaviour of the system is due to the inclusion of small-scale modes, whose energies are orders of magnitude (at least two) less than those of the dominant modes!

Another point that should be noted, when comparing Fig. 9 and Fig. 10 is the direct relation, which is present in all three cases, between the value of the reversal and the total fluctuation energy: a deeper reversal is connected with an increased value of the energy, as one can expect since the dynamo action, which sustains the reversal, is due to the MHD activity.

In the plots of Fig. 11 the distributions of the magnetic energy, given by eq. (17), and of the kinetic energy, given by

$$E_{m,n}^K = \frac{1}{2} \int |\vec{v}_{m,n}|^2 d^3x,$$

of the perturbed spectrum are shown for case *a*: the radius of each circle is proportional to $\log(E_{m,n} \cdot 10^4 / E_{max})$, where $E_{m,n}$ is the magnetic (or kinetic) energy of the (m, n) mode and E_{max} is the maximum magnetic (or kinetic) energy. While in the magnetic spectrum the convergence is satisfactory, i.e. the energy contained in

the high-wave-number part of the spectrum is low, this is not the case for the kinetic spectrum, in which the energy of the $m = 2$ modes is comparable to the energy of the $m = 1$ modes. The previously observed fact that the kinetic energy is larger for the insufficiently resolved case *a* can perhaps be explained by the tendency, due to poor poloidal resolution, towards accumulation of energy in the $m = 2$ modes.

If the resolution is increased (case *b*), the situation shown in Fig. 12 is obtained: here again, even with this finer mesh, good convergence in the kinetic spectrum is not obtained! In particular, it is the poloidal direction which seems to be poorly resolved. In case *c* poloidal mode numbers of up to $m = 5$ are taken into account, the result being shown in Fig. 13. Here, finally, the kinetic spectrum seems to be adequately resolved in m : there is a clear separation between the energy-containing modes $m = 0, 1, 2$ and the small-scale modes $m = 3, 4, 5$. (of course, with high m modes included, the convergence now turns out to be marginal in n : it is like a never-ending story!)

When the magnetic and kinetic energy spectra within a single case are compared, it appears, as far as the dominant modes are concerned, that the magnetic energy is always greater than the kinetic one (and these modes contain by far the major part of the perturbed energy), while for the high-wave-number modes the magnetic and kinetic energies tend to be comparable.

It is useful to introduce the magnetic and kinetic axial spectrum functions, defined as

$$F^M(n) = \sum_m E_{m,n}^M \quad F^K(n) = \sum_m E_{m,n}^K.$$

For case *c* these functions are shown in Fig. 14. It can be seen that in the high- n (both positive and negative) parts of the spectra, the magnetic and kinetic mode energies tend to be equal.

The fact that for high wave numbers the magnetic and kinetic energies are strictly linked is easily shown by modifying the viscosity from $3 \cdot 10^{-4}$ to $9 \cdot 10^{-4}$ and keeping the resistivity constant at $3 \cdot 10^{-4}$. This case is computed with a mesh of $100 \times 12 \times 96$ points, the result being shown in Fig. 15, where for comparison the case with the unmodified viscosity ($3 \cdot 10^{-4}$) is reported too: the higher viscosity produces increased dissipation not only of the kinetic energy but also of the magnetic one and there is equipartition of the energy on small scales. It should be noted that for these Reynolds numbers and the present marginally adequate resolution an inertial range between the energy-containing modes and the dissipation range does not exist.

Coming back to a detailed comparison of the three initial cases, it is useful to

introduce the so-called α coefficient, through which the dynamo electric field is often expressed [3], [13]:

$$\alpha(r) = \langle \delta \vec{v} \times \delta \vec{B} \rangle \cdot \frac{\vec{B}_0}{B_0^2}.$$

In other words, the effect of the fluctuations is taken into account in Ohm's law as an effective parallel electric field $\alpha \vec{B}_0$. The α radial profile can be directly computed from the knowledge of the magnetic and kinetic spectra. The introduction of μ , defined as

$$\mu(r) = \frac{\vec{J}_0 \cdot \vec{B}_0}{B_0^2},$$

which characterizes the mean field distribution, is useful too. μ is the quantity that, in Taylor's theory, characterizes the relaxed state. In this theory μ is constant over the plasma minor radius and is related to the pinch parameter Θ by the relation $\mu a = 2\Theta$. Cylindrically symmetric Bessel function states are minimum energy states for $\mu a < 3.11$; when 3.11 is reached, the minimum energy state is helically deformed and Θ saturates at 1.55. The limitation on Θ predicted by the theory is not observed experimentally: values of Θ like that adopted here, 1.7, are currently being reached in experiments. Furthermore, the μ profile is observed to vanish at the wall. This discrepancy is generally ascribed to the boundary conditions: in a real experiment the current density close to the wall is very small, while the constancy of μ implies a current density very different from zero. In the present simulation, too, the resistivity profile acts in such a way as to have a small current density, i.e. small μ , at the wall.

In Fig. 16 the time-averaged radial profiles of the coefficients α and μ , for the three cases, are shown. As regards α , cases *b* and *c* give essentially the same result, while case *a* differs considerably. In the present formulation α vanishes at the wall owing to the boundary conditions for the velocity fields. Note that in the three cases the peaking of the α profile is located around $r \approx 0.8$, which corresponds to the position of the reversal, and that in case *a* the less pronounced reversal corresponds to a lower value of α . In the μ profile the differences are less marked and the three cases look quite similar: μ tends to be flat in the inner region and is very close to zero at the wall.

The kind of α profile shown, negative in the internal region and positive in the outer one, characterizes the quasi-stationary turbulent state. As reported by Strauss [13], it is this form of α which tends to flatten the current profile, i.e. μ , in the inner region. α redistributes the current but does not sustain it in a quasi-steady state.

In some studies [14,15] the electromotive mean field generated by the turbulence, $\vec{\mathcal{E}} = \langle \delta \vec{v} \times \delta \vec{B} \rangle$, has been connected with the conservation properties of the plasma.

In particular, it has been shown /15/ that $\vec{\mathcal{E}}$ satisfies two properties:

$$\int \vec{\mathcal{E}} \cdot \vec{B}_0 d^3x = \int \alpha B_0^2 d^3x = 0$$

and

$$\int \vec{\mathcal{E}} \cdot \vec{J}_0 d^3x < 0,$$

both correct to $O(\eta)$. The turbulent fields $\vec{\mathcal{E}}$ obtained from the code satisfy these relations in very good approximation. This means that, since the magnetic helicity and the magnetic energy dissipations are given by

$$\frac{dK_{diss}^M}{dt} = 2 \int \vec{E} \cdot \vec{B} d^3x \quad \frac{dE_{diss}^M}{dt} = \int \vec{E} \cdot \vec{J} d^3x,$$

the fluctuations, to $O(\eta)$, do not dissipate magnetic helicity but they dissipate magnetic energy.

4.3. Higher Reynolds Numbers

In this section some results regarding Reynolds numbers higher than those considered so far are presented. This is done while keeping in mind the results on the limits of the spectral resolution in the previous section.

Of particular interest is the study of the behaviour of the magnetic and kinetic fluctuations as the Reynolds numbers are increased. In fact, as the resistivity decreases, the electromotive field $\vec{\mathcal{E}}$, which is the product of the kinetic and magnetic fluctuations, is expected to do the same since in steady-state (or quasi-steady-state) conditions $\vec{\mathcal{E}}$ should be proportional to $\eta \vec{J}$. But theories able to predict the behaviour of the magnetic and kinetic fluctuations separately do not exist. Fluctuation levels are important in the RFP configuration because of their possible effects on the transport. In particular, the behaviour of the magnetic fluctuations is crucial: some typical transport coefficients, such as the anomalous electron thermal conductivity, are expected to be proportional to the square of the relative amplitude $\delta B/B$ of the magnetic fluctuations.

Two cases, with Reynolds numbers 10^4 and $3.3 \cdot 10^4$, are considered here. The total magnetic and kinetic energies of the perturbation are taken as a measure of the global fluctuation level. The case with both the resistivity and the viscosity at 10^{-4} is studied first, a resolution of $100 \times 12 \times 96$ being used. The initial state is the one cited at the end of Section 4.1 and the case is computed up to $t = 1200$.

The time evolution of the field reversal parameter is shown in Fig. 17: F manifests irregular oscillatory behaviour. The perturbed spectrum is characterized by intense mode activity, as shown in Fig. 18 for the $m = 1$ internal modes, which are the most energetic. The resulting magnetic and kinetic spectra, averaged in time, are shown in Fig. 19: when this figure is compared with Fig. 12, which refers to the previous case with the same mesh, it can be seen that the convergence now obtained is still satisfactory although the energy now is more spread among the small-scale modes. In Fig. 20 the corresponding axial spectral functions $F^M(n)$ and $F^K(n)$ are given. As regards the radial mesh, the number of points employed gives good resolution, as shown in Fig. 21, where a contour plot of the axial current density J_z , at the time $t = 900$ is given.

In Fig. 22 the time evolution of the magnetic and kinetic energies of the perturbation are shown. It can be seen that the first part of the evolution, up to $t \approx 400$, is characterized by large fluctuations, in particular in the magnetic energy, and it resembles a sort of relaxation process toward a lower energy level. It must be remembered in fact that the initial state corresponds to a $3 \cdot 10^{-4}$ case, very likely characterized by higher energy level than the present one. After the initial stage the magnetic energy is again subject to oscillatory behaviour, but with a smaller amplitude.

In Fig. 23 time averages of the mean magnetic field and of the μ coefficient are shown. All these averages are taken between $t = 500$ and $t = 1200$. The μ profile is flat in the central region, up to $r \approx 0.5$, the flat part reaching further out than in the previous cases (cf. Fig. 16). This means that, at least in the inner region of the plasma, the mean magnetic field is well described by the Bessel function model. Furthermore, it should be noted that the "plateau" value is very close to $3.4 = 2\Theta$, i.e. the constant value which, owing to the boundary conditions, μ should assume according to the Bessel function model.

The case with resistivity and viscosity at $3 \cdot 10^{-5}$ is treated in a somewhat different way. Using a resolution of $100 \times 12 \times 96$, one must obviously expect in this case a substantial accumulation of energy in the high-mode-number part of the spectra. To avoid, this the diffusion coefficients η and ν are modified by introducing a dependence on the mode numbers:

$$g(m, n) = 1 + \left(\frac{m}{m_0}\right)^4 + \left(\frac{n}{n_0}\right)^4,$$

where m_0 and n_0 are constant. m_0 and n_0 are chosen such as to increase the dissipation of energy for the small-scale modes and to leave the energy-containing modes

essentially unaffected. With the characteristic spectra of the problem being taken into account, the values $m_0 = 3$ and $n_0 = 25$ are used. Of course, such a procedure is strongly questionable without any other detailed study of the effect of the small-scale modes. But it is very likely that the results obtained in this way are in some sense more “realistic” than those that would be obtained with the unmodified diffusion coefficients.

This case is computed up to $t = 1400$. In Fig. 24 the time evolutions of the reversal parameter and of the total magnetic and kinetic energies of the perturbation are shown. After an initial relaxation phase, up to $t \approx 600$, characterized by a large-amplitude oscillation, the reversal and the energies assume the usual irregular oscillatory behaviour. The magnetic and kinetic energy spectra are given in Fig. 25: it is clear that the artificial resistivity and viscosity employed have avoided the accumulation of energy in the small-scale modes, allowing one to obtain rather good convergence in both the poloidal and axial directions. The question of the reliability of this procedure remains open and more investigations are necessary to clarify this point.

The results so far shown afford an indication of the possible scalings of the fluctuations with the Reynolds numbers. The term “indication” should be carefully noted.

Considering the time evolutions of the perturbation energies in the three cases with diffusion coefficients $3 \cdot 10^{-4}$ (Fig. 10), 10^{-4} (Fig. 22), and $3 \cdot 10^{-5}$ (Fig. 24) and making the appropriate time averages yields the result given in Fig. 26. As the Reynolds numbers increase the magnetic perturbation decreases, while the behaviour of the kinetic perturbation does not show any clear tendency. It should be remembered in fact, from Section 4.2, that the value of the perturbed kinetic energy is the more sensitive to the resolution and for this reason further conclusions regarding the kinetic part will not be drawn here. As regards the magnetic perturbation, the result for the $3 \cdot 10^{-5}$ case, which is the most uncertain one, fits well with the other two cases.

If a power law of the type $E^M \propto (R^M)^\delta$ is supposed, a value of -0.6 for the exponent δ is obtained. Since E^M is, roughly speaking, proportional to $(\delta B/B)^2$, the magnetic fluctuations are found to scale as $\delta B/B \propto (R^M)^{-0.3}$.

5. Conclusions

The computations presented in this work show that the main feature of the reversed field pinch configuration, i.e. the maintenance of the toroidal field reversal, can be explained within the framework of single-fluid resistive magnetohydrodynamics. The reversal can be maintained in time, against resistive decay, by an externally applied toroidal electric field. Here the boundary condition of constant poloidal magnetic field at the wall, which in general implies a non-vanishing toroidal electric field, has been used. The role of the fluctuations is to produce an electric field which redistributes the current in the plasma and sustains the reversal.

Although the qualitative features of the RFP behaviour can be well reproduced by these 3D MHD simulations, it is a major problem in dealing with these equations to obtain an accurate solution, even at moderate values of the Reynolds numbers. This is due to the turbulent nature of the problem, which leads to the excitation of smaller and smaller scales.

The results presented here seem to support the fact that, to obtain an accurate solution, all the scales of the problem, from the energy-containing range to the dissipative range, must be properly resolved. It has been shown that, at low Reynolds numbers such as $3.3 \cdot 10^3$, the inclusion of small-scale modes can have a strong effect on a macroscopic parameter like F and on the energy content of the perturbation. The energy contained in the small-scale modes is negligible, but very likely these modes affect the dynamics of the system through a modification of the effective resistivity and viscosity felt by the large scales /16,17,18/.

A direct simulation of the small-scale modes is only possible at relatively low Reynolds numbers. As the Reynolds numbers increase the typical dissipation length scale decreases and therefore an increasing number of modes must be taken into account, so that the simulation of all the scales involved soon becomes prohibitive. High Reynolds numbers therefore require a distinct treatment of the large scales and of the small scales. Like hydrodynamics /19,20/, MHD would also require subgrid modelling of the effects of the small scales on the energy-containing scales. But, unfortunately, such techniques are not yet well developed in MHD /21/.

A simpler approach could be afforded by a particular treatment of the dissipative terms in the equations, through modified diffusion coefficients or higher-order differential operators. Such artificial terms avoid the accumulation of energy in the high-mode-number part of the spectrum, which would otherwise be present with the

use of the classical dissipative terms. An example of this approach has been given by treating the $3 \cdot 10^{-5}$ case.

Some results of a study of the fluctuation behaviour with the Reynolds numbers have been presented. While the $R^M = 3.3 \cdot 10^3$ case has been investigated in detail, the results for the other two cases, $R^M = 10^4$ and $3.3 \cdot 10^4$, must be considered preliminary. As the dissipations decrease the magnetic fluctuations, too, are found to decrease, though not very strongly, $\delta B/B \propto (R^M)^{-\frac{1}{3}}$.

Acknowledgements

One of the authors (D. Merlin) thanks M. Walter and H. Welter for their continuous support and advice on the computer system, and IPP for the kind hospitality accorded to him.

References

- 1 - J.B. Taylor, Phys. Rev. Lett. **33**, 1139 (1974).
- 2 - H.K. Moffatt, "Magnetic Field Generation in Electrically Conducting Fluids", Cambridge U.P., Cambridge, 1978.
- 3 - F. Krause and K.H. Rädler, "Mean-Field Magnetohydrodynamics and Dynamo Theory", Pergamon, Oxford, 1980.
- 4 - S. Ortolani, "Magnetic Confinement in Reversed Field Pinch Plasmas" in Proc. of 1987 International School of Plasma Physics, Course on Physics of Mirrors, Reversed Field Pinches and Compact Tori, Varenna, Italy.
- 5 - E.J. Caramana, R.A. Nebel, D.D. Schnack, Phys. Fluids **26**, 1305 (1983).
- 6 - A.Y. Aydemir and D.C. Barnes, Phys. Rev. Lett. **52**, 930 (1984).
- 7 - D.D. Schnack, E.J. Caramana, R.A. Nebel, Phys. Fluids **28**, 321 (1985).
- 8 - D.D. Schnack et.al., J. Comp. Phys. **70**, 330 (1987).
- 9 - D. Gottlieb and S.A. Orszag, Numerical Analysis of Spectral Methods, SIAM, Philadelphia, 1977.
- 10 - D.S. Harned and W. Kerner, J. Comp. Phys. **60**, 62 (1985).
- 11 - D.S. Harned and D.D. Schnack, J. Comp. Phys. **65**, 57 (1986).
- 12 - A.J. Robert, in Proceedings of WMO/IUGG Symposium on Numerical Weather Predictions, Tokyo, 1969.
- 13 - H.R. Strauss, Phys. Fluids **28**, 2786 (1985).
- 14 - A.H. Boozer, J. Plasma Phys. **35**, 133 (1986).
- 15 - E. Hameiri and A. Bhattacharjee, Phys. Fluids **30**, 1743 (1987).
- 16 - A. Pouquet, J. Fluid Mech. **88**, 1 (1978).
- 17 - D. Biskamp, Plasma Phys. Contr. Fusion. **26**, 311 (1984).
- 18 - P.H. Diamond, R.D. Hazeltine, Z.G. An, B.A. Carreras and H.R. Hicks, Phys. Fluids **27**, 1449 (1984).
- 19 - J. Smagorinsky, Mon. Weather Rev. **91**, 99 (1963).
- 20 - V. Yakhot, S.A. Orszag, J. Sci. Comput. **1**, 3 (1986).

21 - A. Yoshizawa, Phys. Fluids **30**, 1089 (1987).

Figure Captions

- Fig. 1 - Time evolution of the field reversal parameter for the pure axisymmetric case.
- Fig. 2 - Time evolution of the term $E_z B_\theta$ at the wall.
- Fig. 3 - Time evolution of the field reversal parameter for the case $\eta = 10^{-3}$ and $R = 1$.
- Fig. 4 - Time evolutions of the magnetic energies of the modes for the case $\eta = 10^{-3}$ and $R = 1$. (a) internal modes $m = 1, 2; n = -1, -5$. (b) external modes $m = 1, 2; n = 0, 5$. (c) $m = 0; n = 1, 5$ modes.
- Fig. 5 - Time evolution of the field reversal for the case $\eta = 3 \cdot 10^{-4}$ and $R = 2$.
- Fig. 6 - Time evolutions of the magnetic energy of the internal modes ($m = 1, 2; n = -1, -10$) for the case $\eta = 3 \cdot 10^{-4}$ and $R = 2$.
- Fig. 7 - Radial profiles of the terms in the poloidal component of Ohm's law. (1) poloidal voltage $\eta J_{\theta 0}$; (2) $v_{r0} B_{z0}$ term; (3) fluctuation term; the dotted line indicates the poloidal electric field.
- Fig. 8 - Radial profiles of the time-averaged mean magnetic fields for case c .
- Fig. 9 - Time evolutions of the reversal parameter (line marked by crosses - case a ; dotted line - case b ; solid line - case c).
- Fig. 10 - Time evolutions of the total magnetic (a) and kinetic (b) energies of the perturbation (lines marked by crosses - case a ; dotted lines - case b ; solid lines - case c).
- Fig. 11 - Distributions of the magnetic and kinetic energies for case a .
- Fig. 12 - Distributions of the magnetic and kinetic energies for case b .
- Fig. 13 - Distributions of the magnetic and kinetic energies for case c .
- Fig. 14 - Axial spectral functions $F^M(n)$ and $F^K(n)$ for case c .
- Fig. 15 - Axial spectral functions $F^M(n)$ and $F^K(n)$ for the case $\nu = 3 \cdot 10^{-4}$ (a) and $\nu = 9 \cdot 10^{-4}$ (b).
- Fig. 16 - Radial profiles of α (a) and μ (b) (lines marked by crosses - case a ; dotted lines - case b ; solid lines - case c).
- Fig. 17 - Time evolution of the field reversal parameter for the case $\eta = 10^{-4}$.

- Fig. 18 - Time evolutions of the magnetic (a) and kinetic (b) energies of the $m = 1$ internal modes for the case $\eta = 10^{-4}$.
- Fig. 19 - Distributions of the magnetic and kinetic energies for the case $\eta = 10^{-4}$.
- Fig. 20 - Axial spectral functions $F^M(n)$ and $F^K(n)$ for the case $\eta = 10^{-4}$.
- Fig. 21 - Contour plot of the axial current density J_z at the time $t = 900$ for the case $\eta = 10^{-4}$.
- Fig. 22 - Time evolutions of the total magnetic (upper curve) and kinetic (lower curve) energies of the perturbation for the case $\eta = 10^{-4}$.
- Fig. 23 - Radial profiles of the time-averaged mean magnetic fields (a) and μ (b) for the case $\eta = 10^{-4}$.
- Fig. 24 - Time evolutions of the field reversal parameter (a) and of the total magnetic and kinetic energies of the perturbation (b) for the case $\eta = 3 \cdot 10^{-5}$.
- Fig. 25 - Distributions of the magnetic and kinetic energies for the case $\eta = 3 \cdot 10^{-5}$.
- Fig. 26 - Time-averaged total magnetic (crosses) and kinetic (diamonds) energies of the perturbation as functions of the Reynolds numbers ($R = R^M = R^K$).

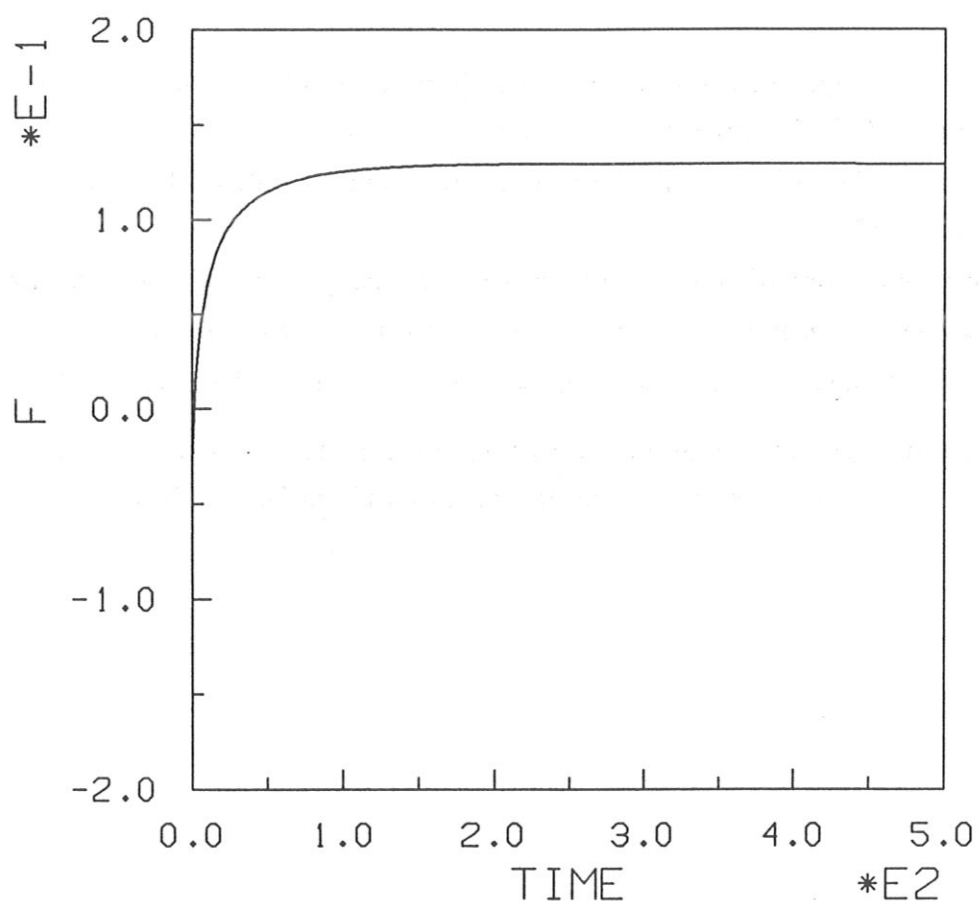


Fig. 1

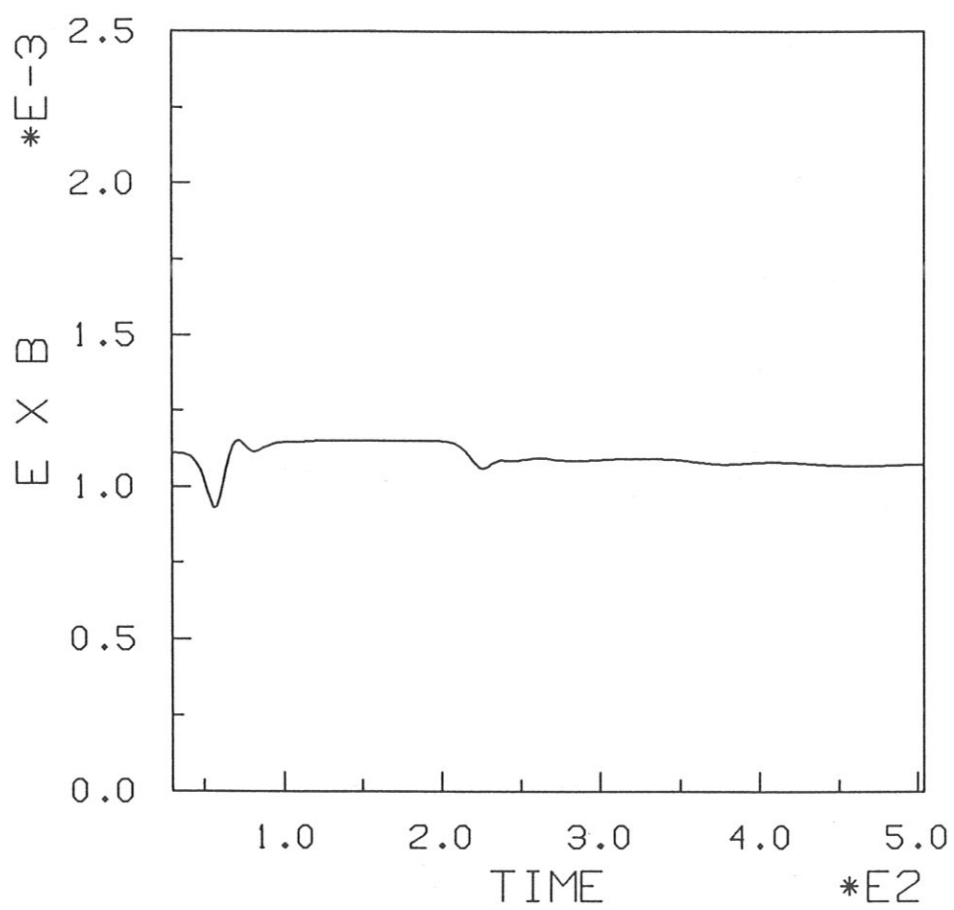


Fig. 2

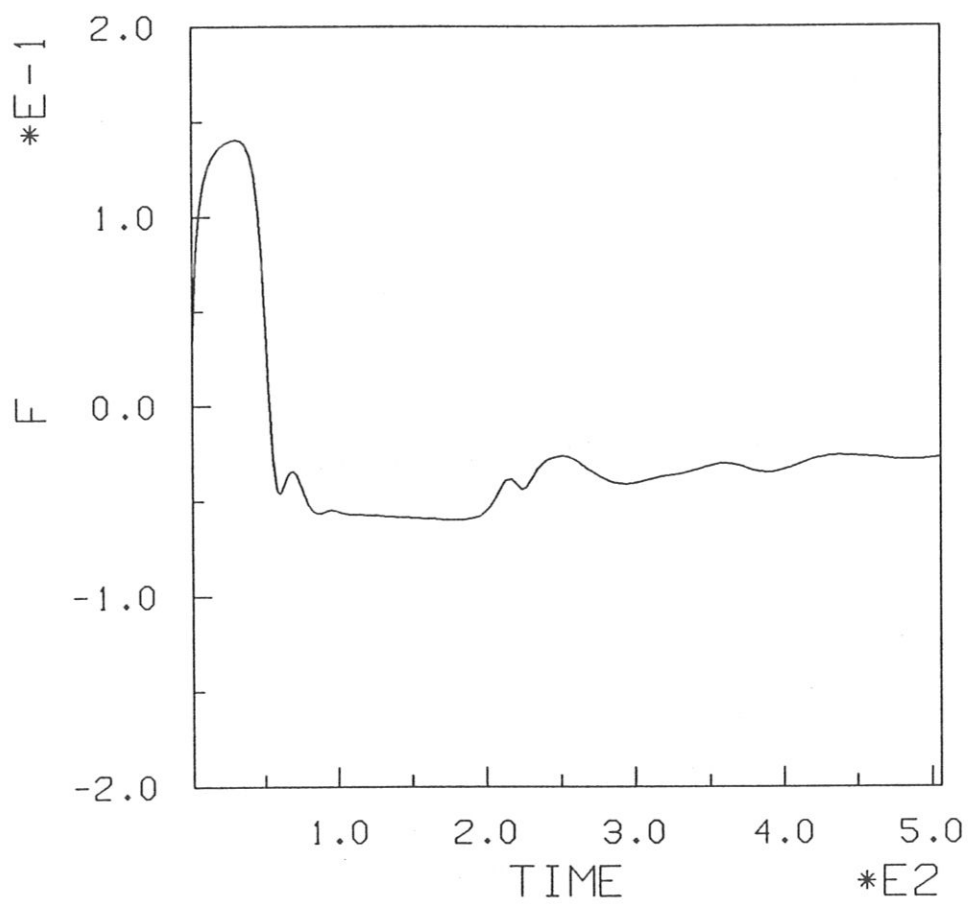
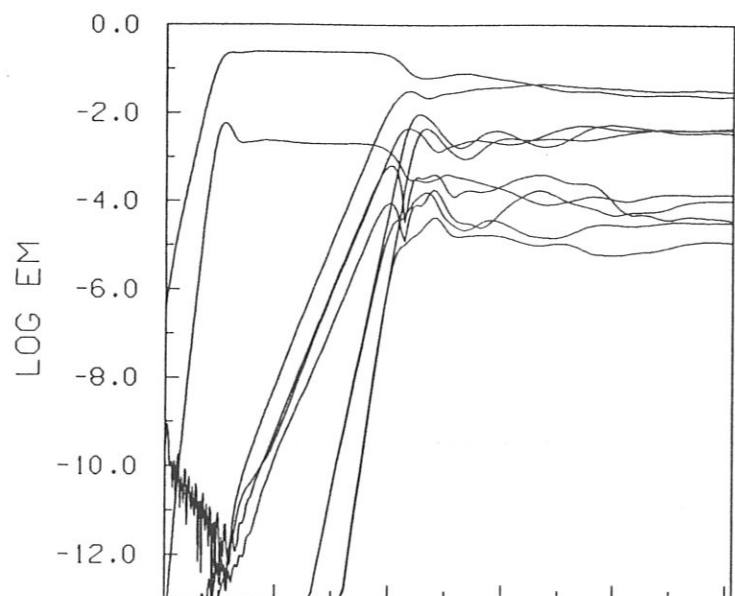
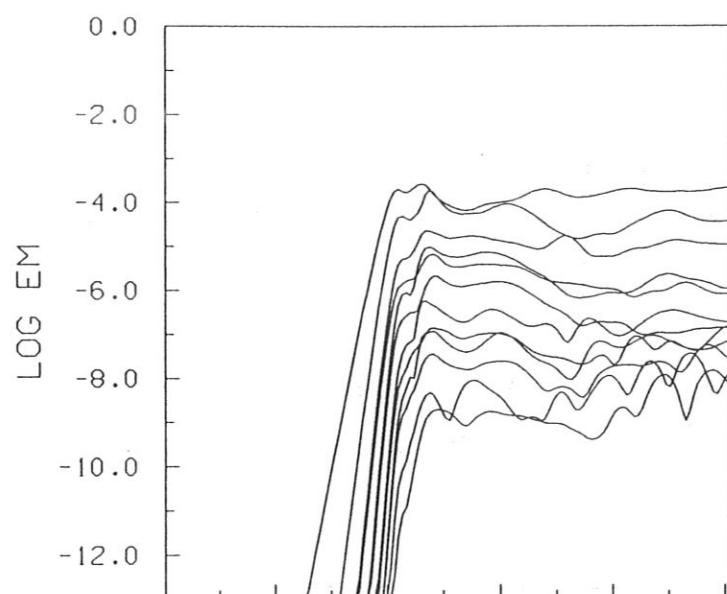


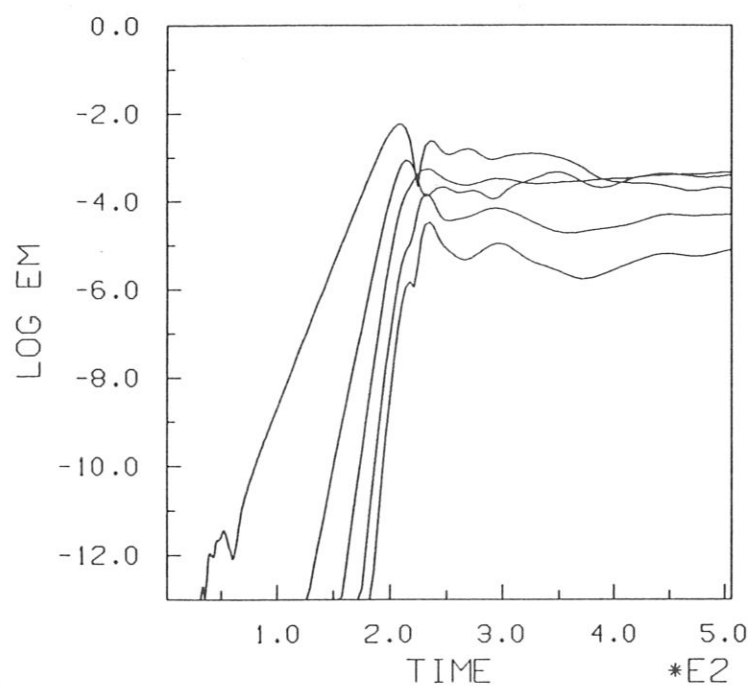
Fig. 3



a)



b)



c)

Fig. 4

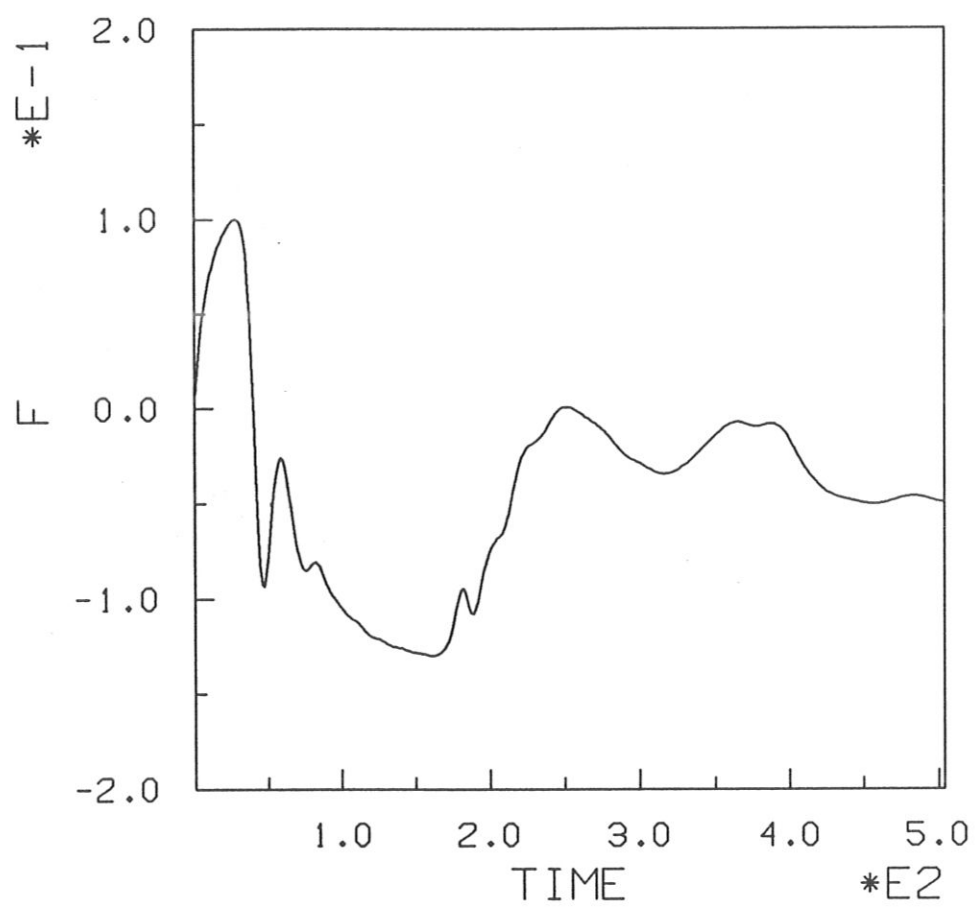


Fig. 5

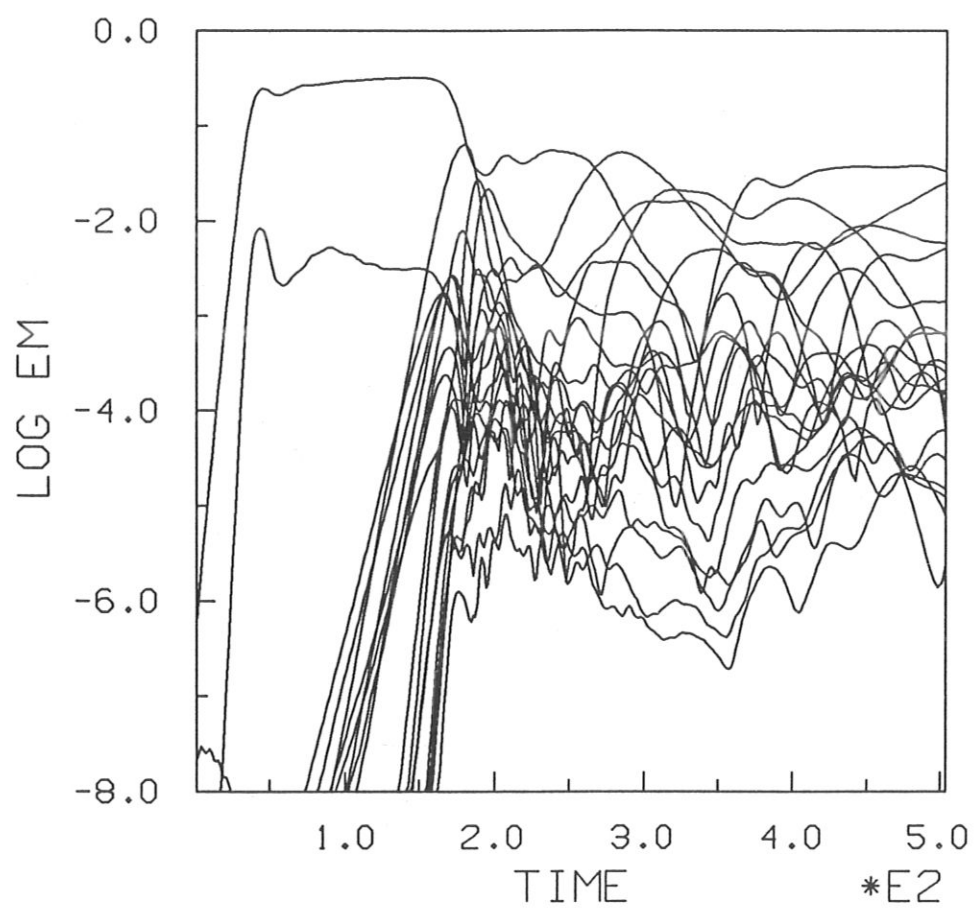


Fig. 6

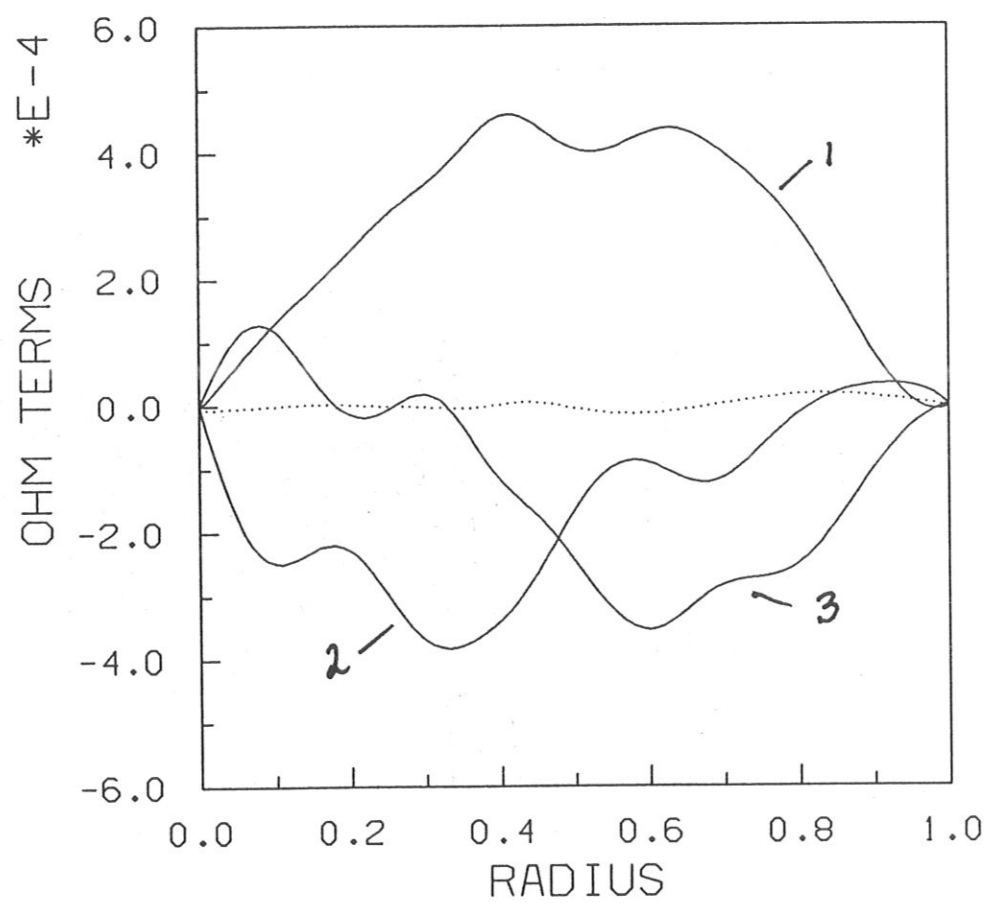


Fig. 7

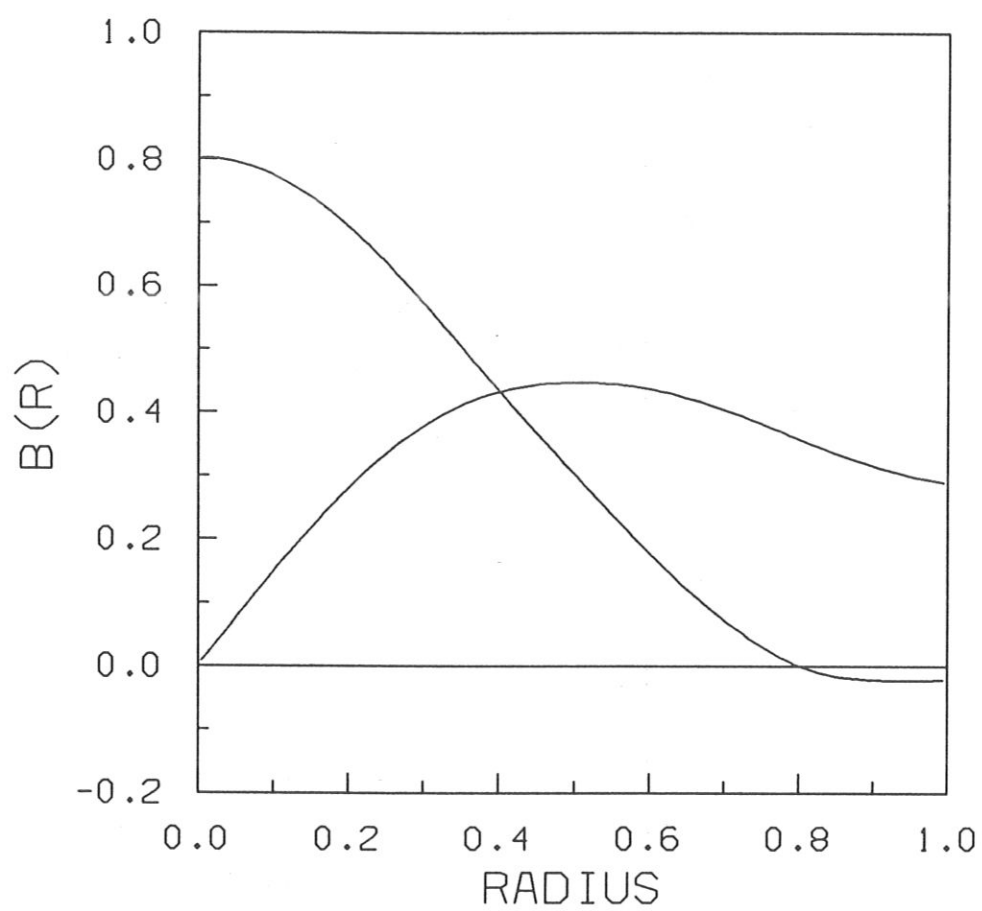


Fig. 8

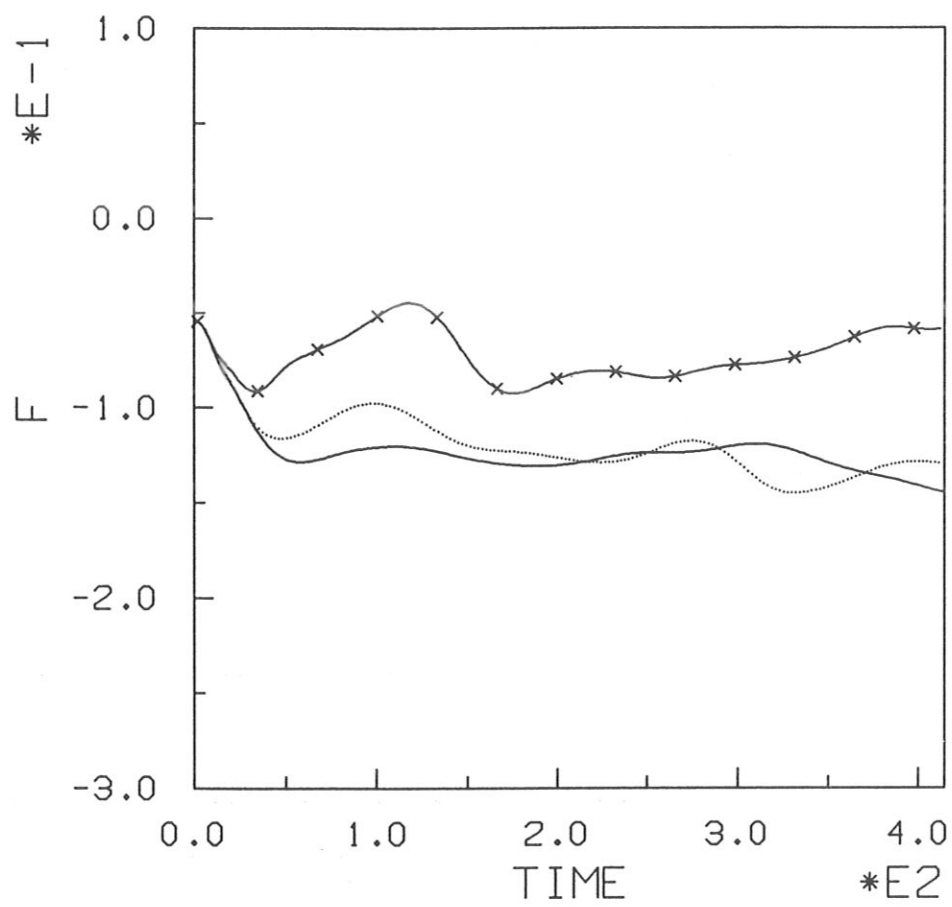


Fig. 9

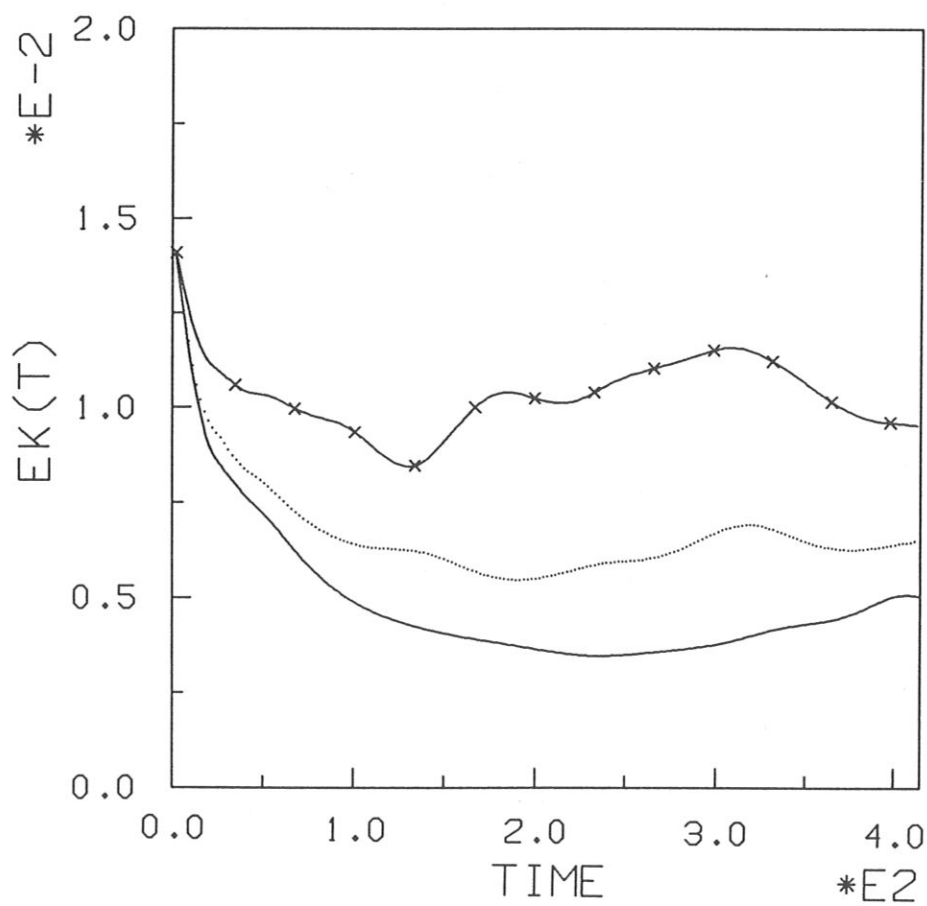
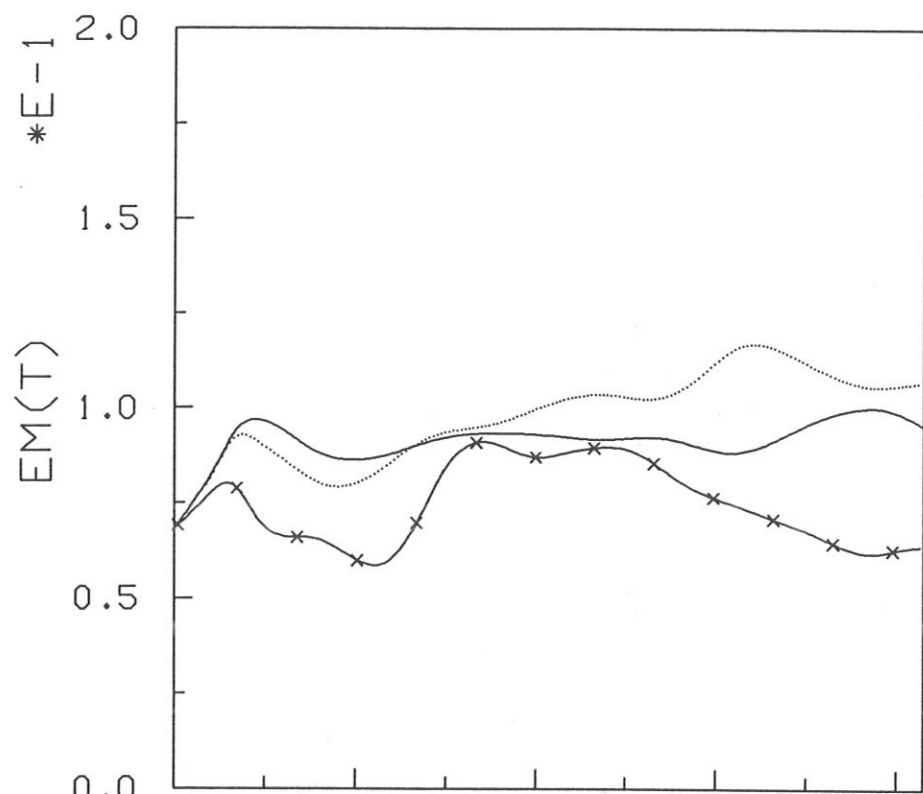


Fig. 10

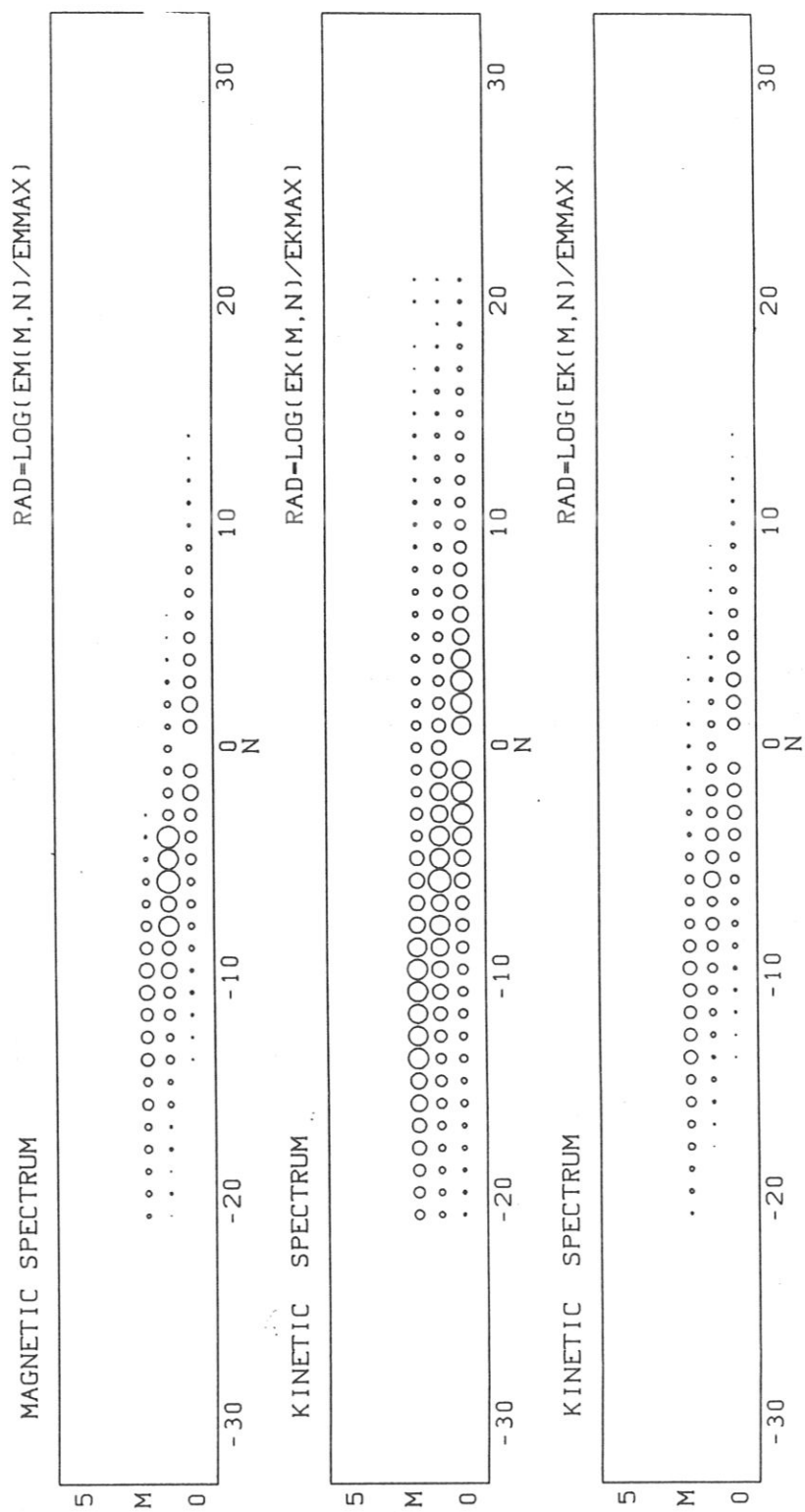


Fig. 11

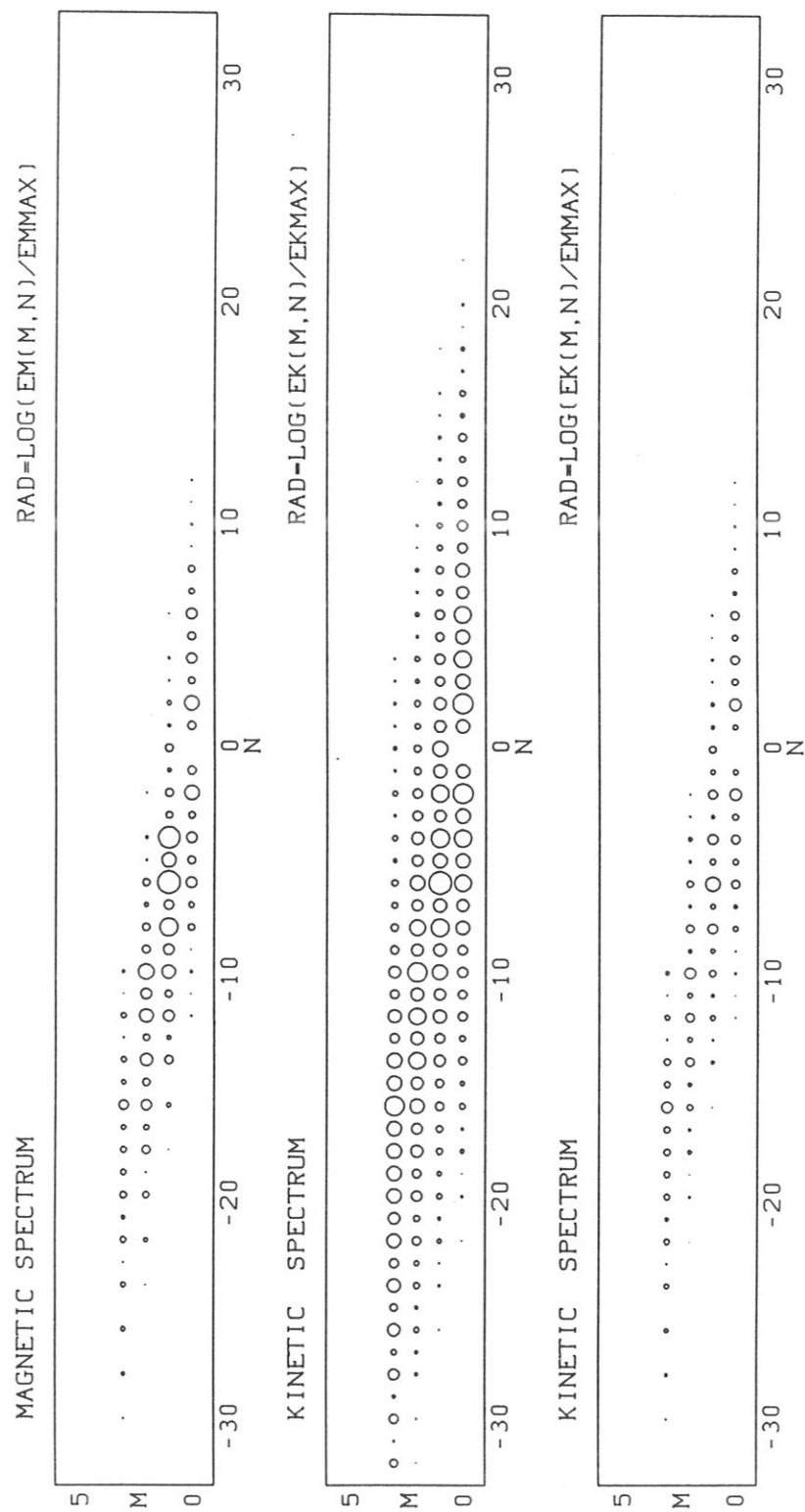


Fig. 12

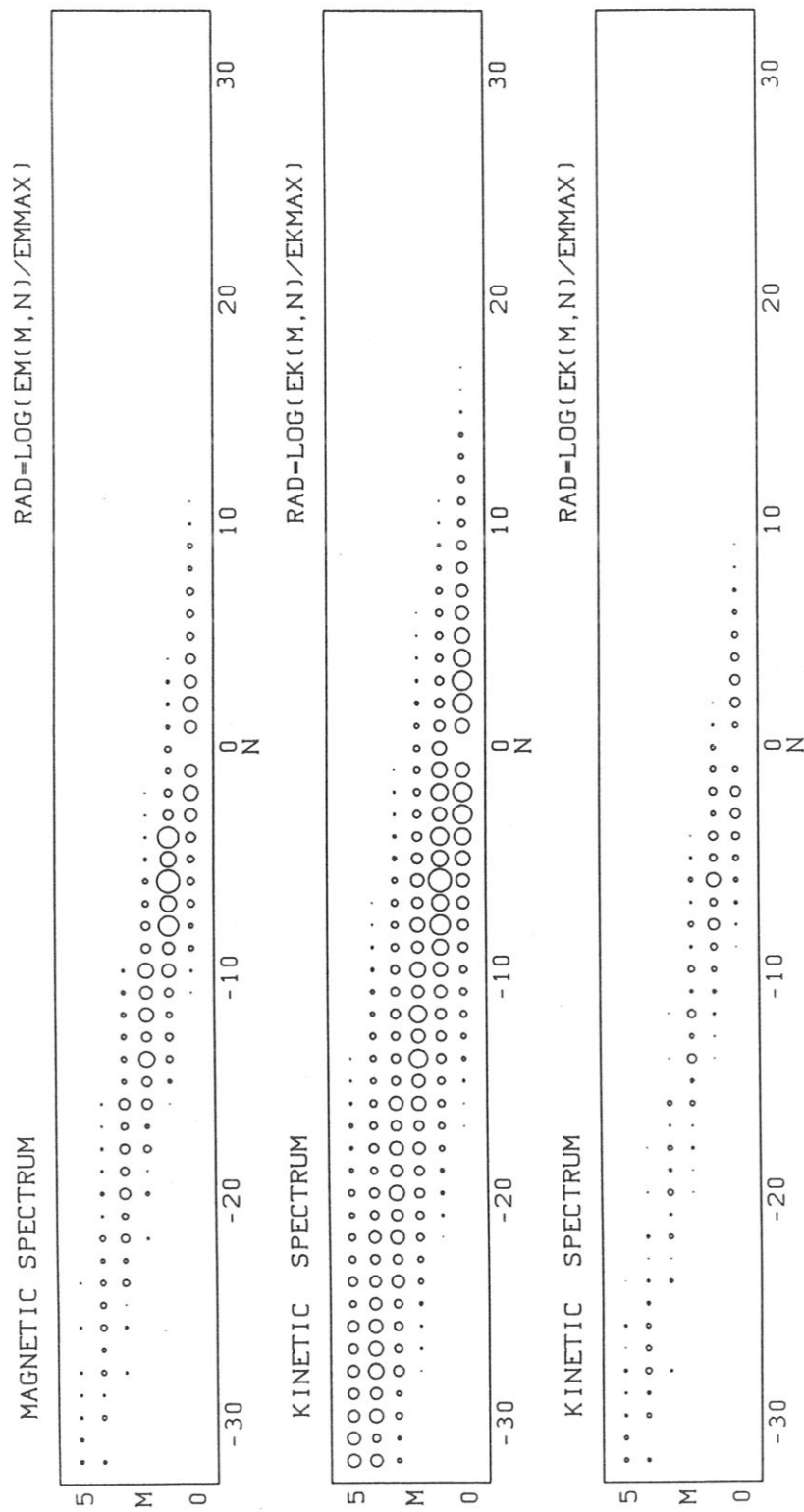


Fig. 13

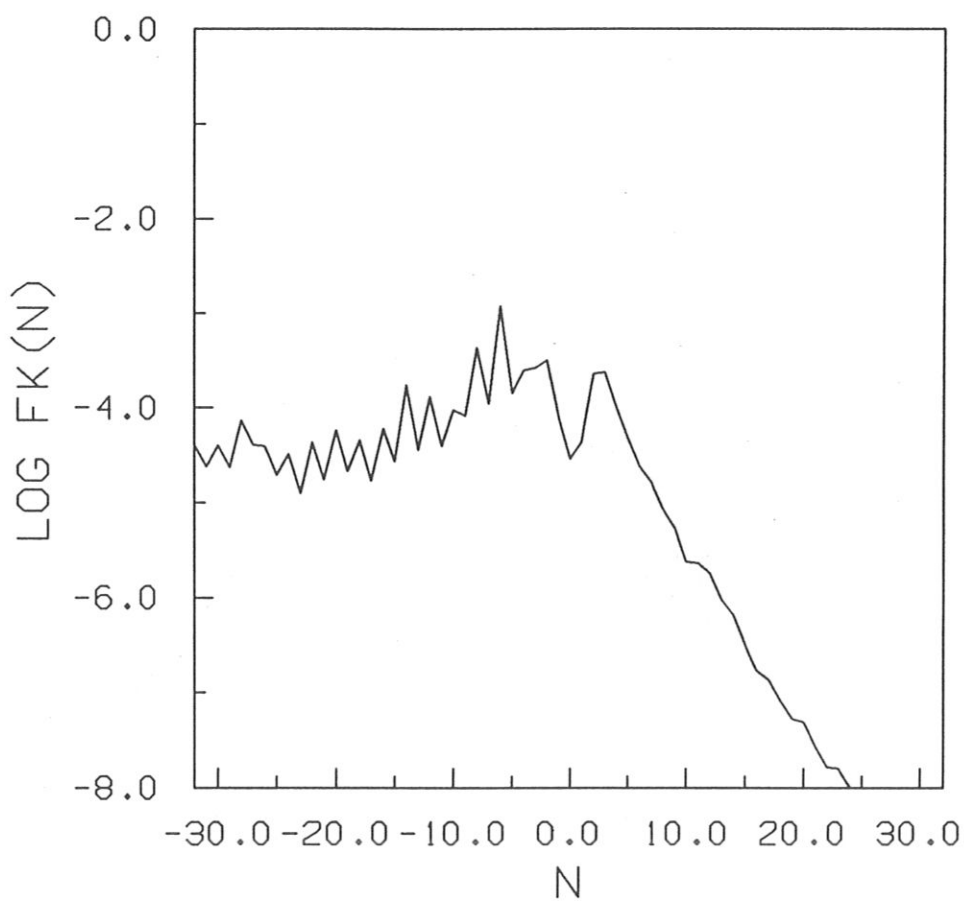
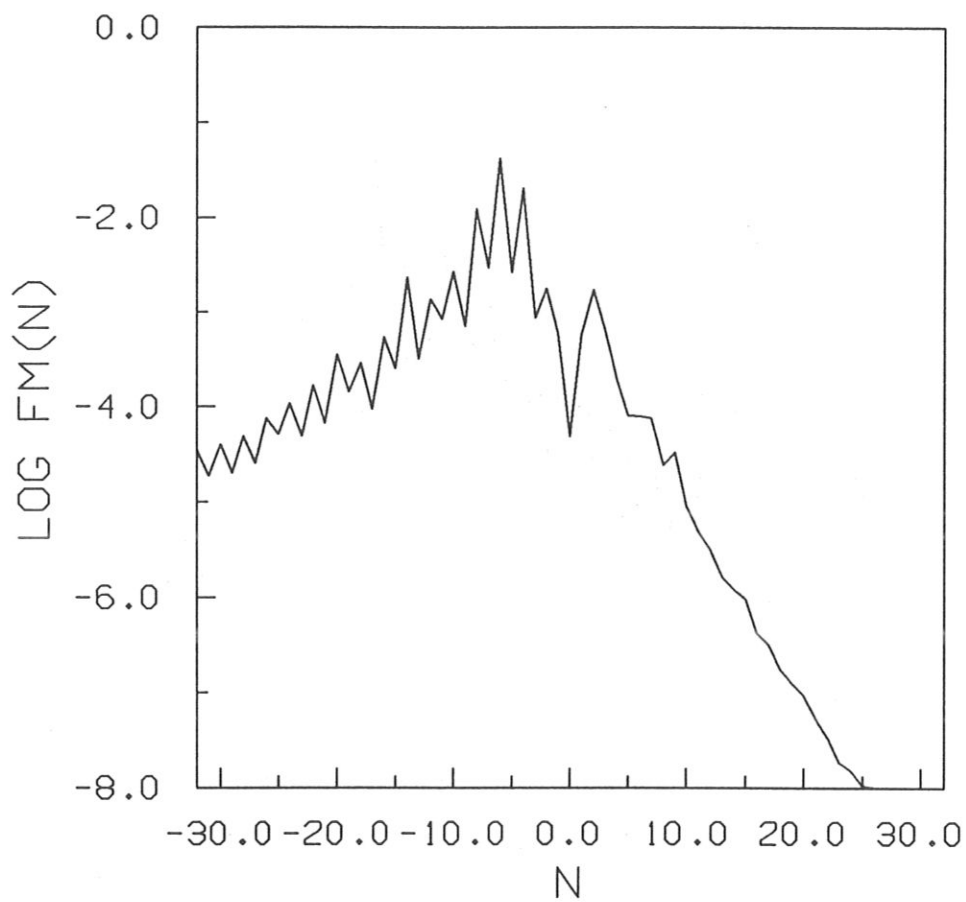


Fig. 14

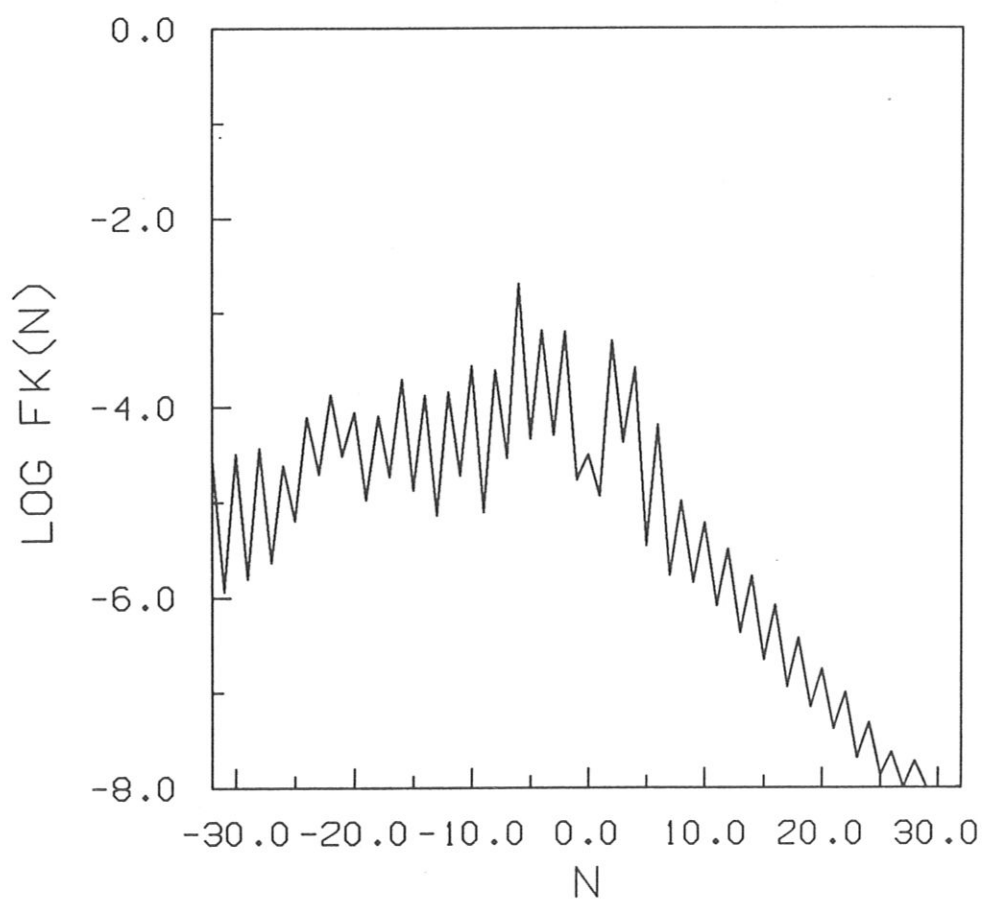
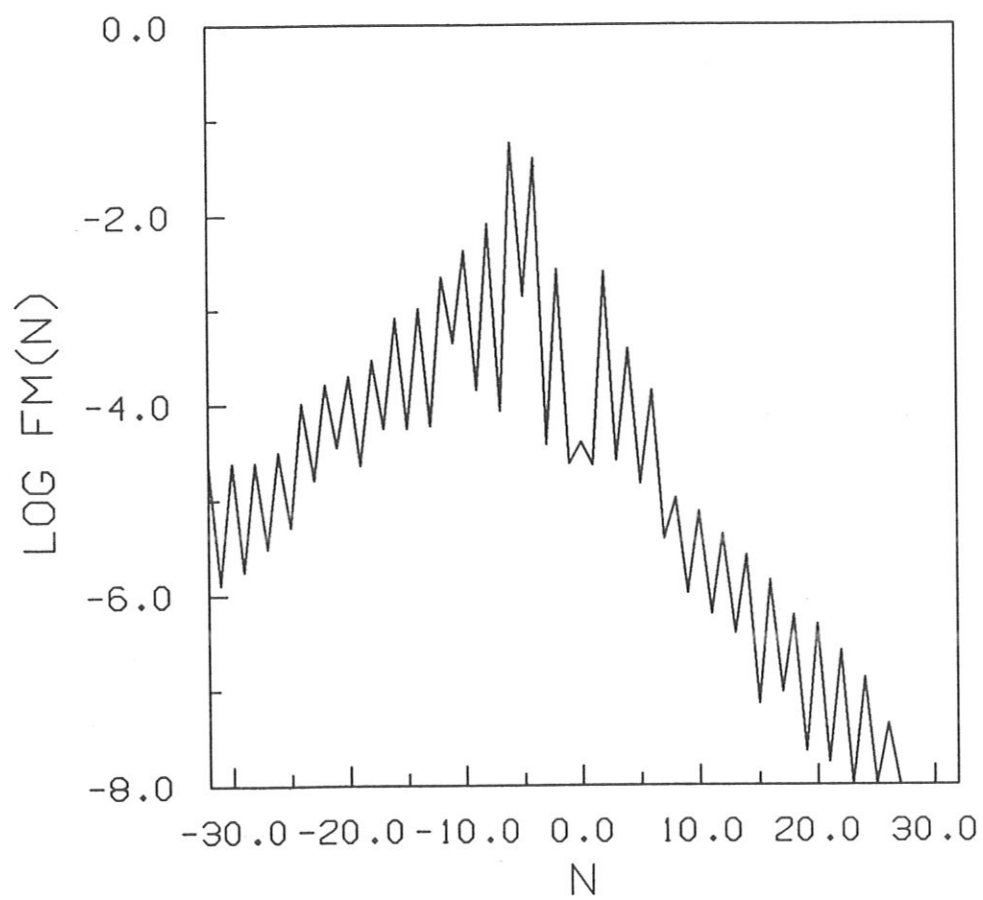


Fig. 15a

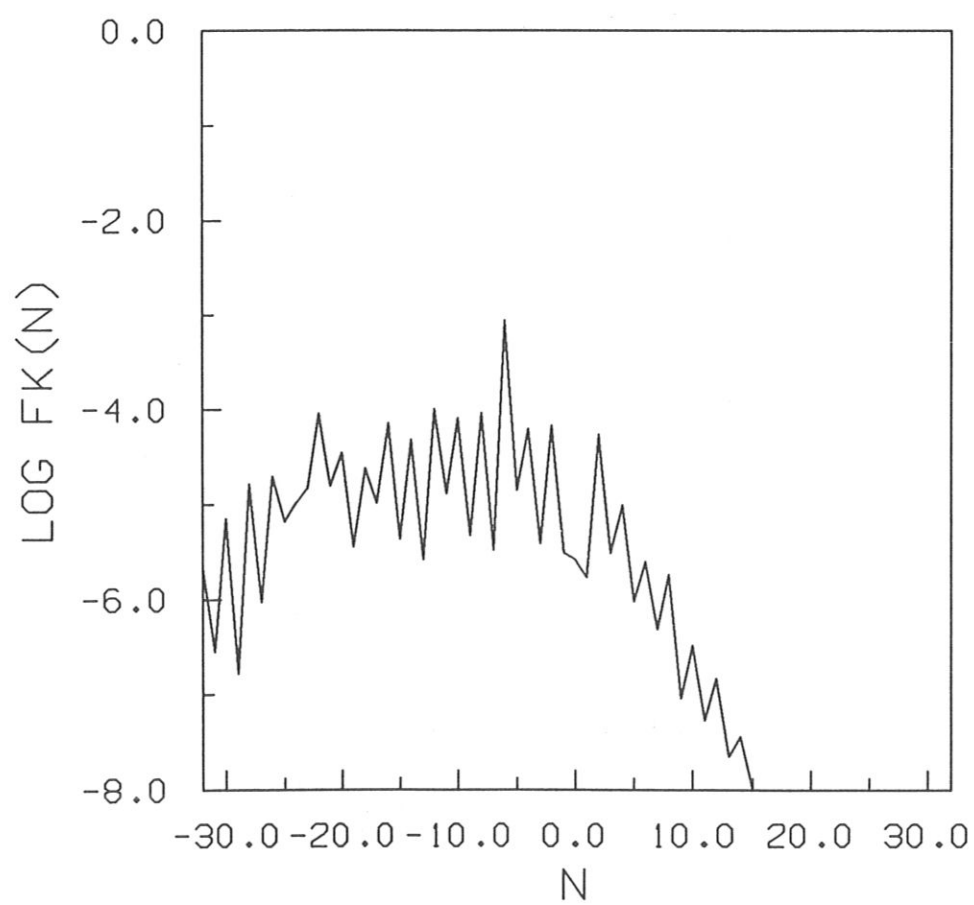
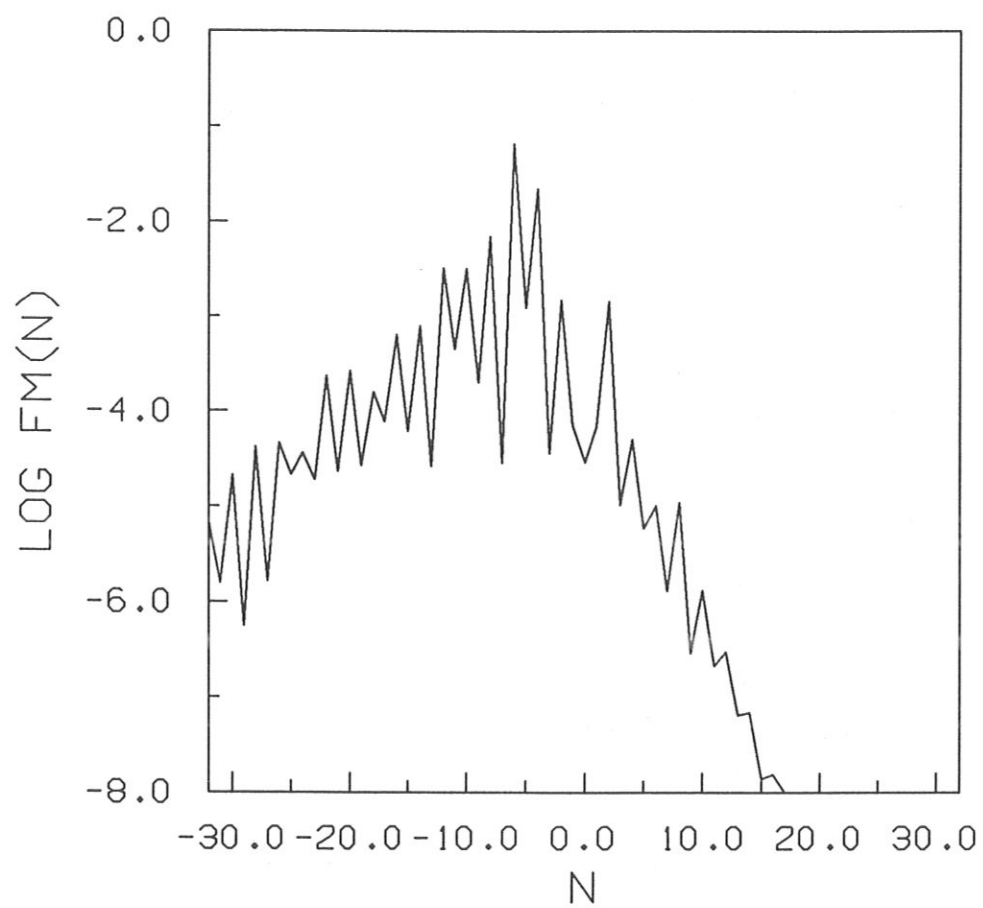


Fig. 15b

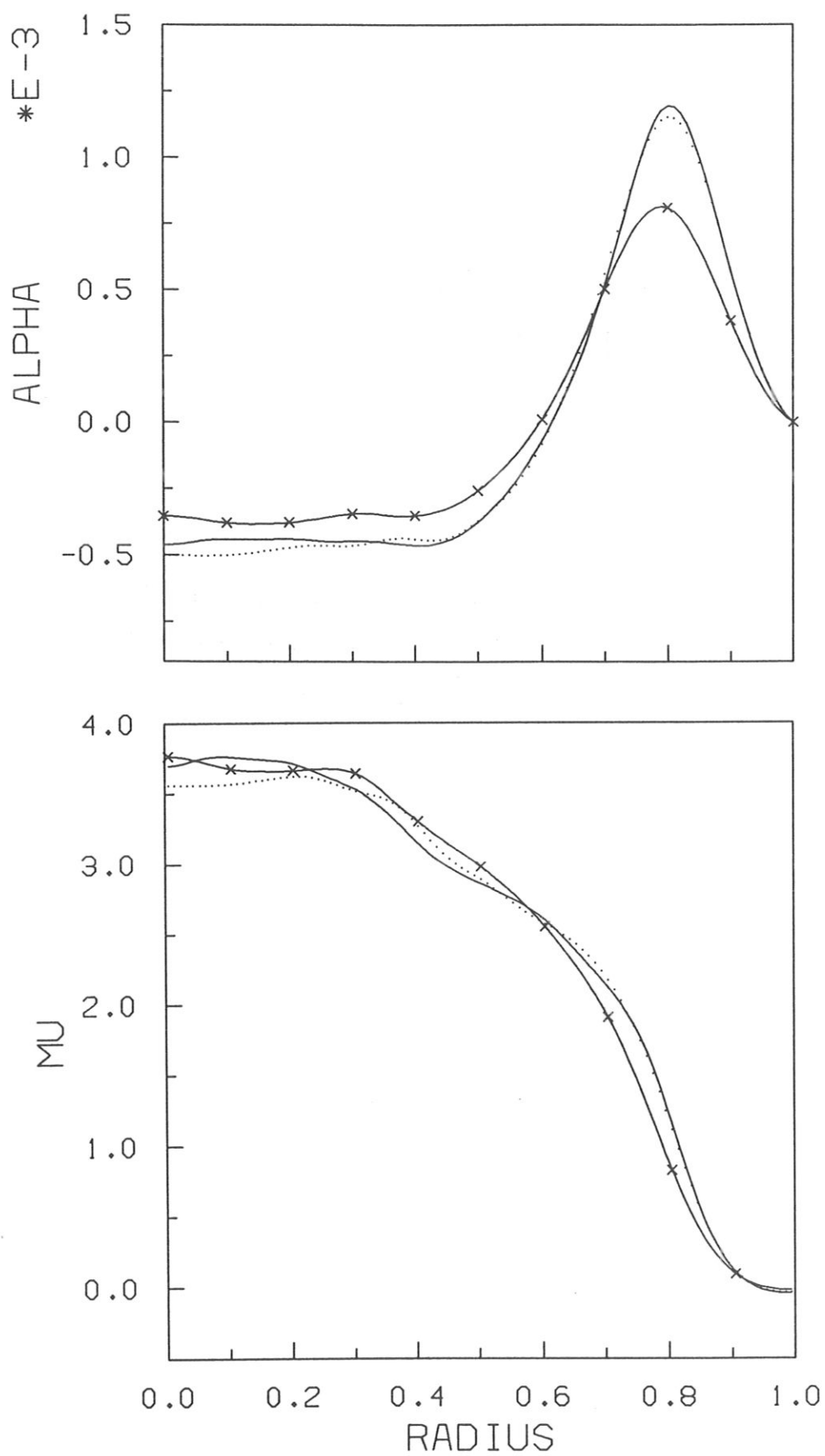


Fig. 16

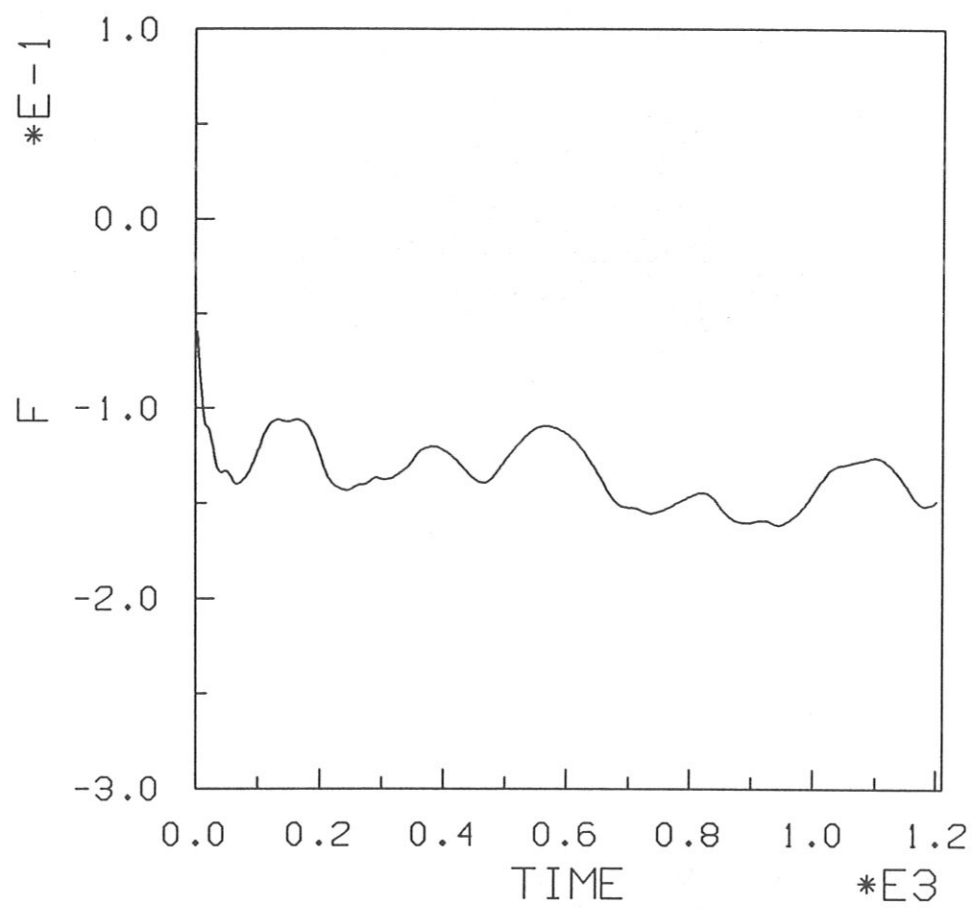
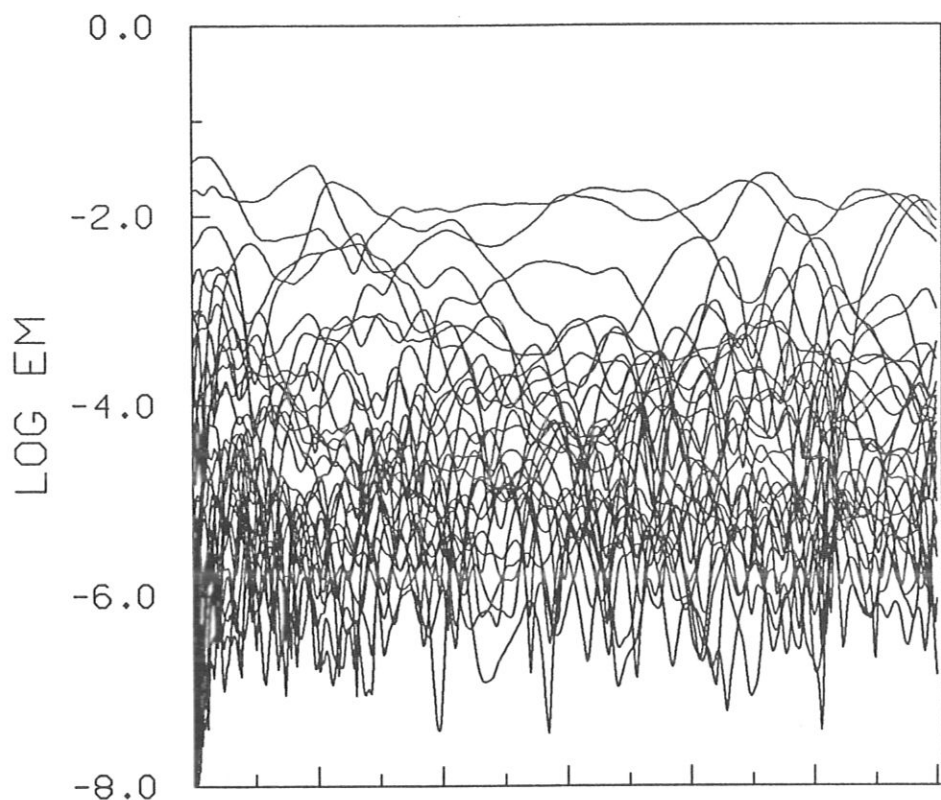
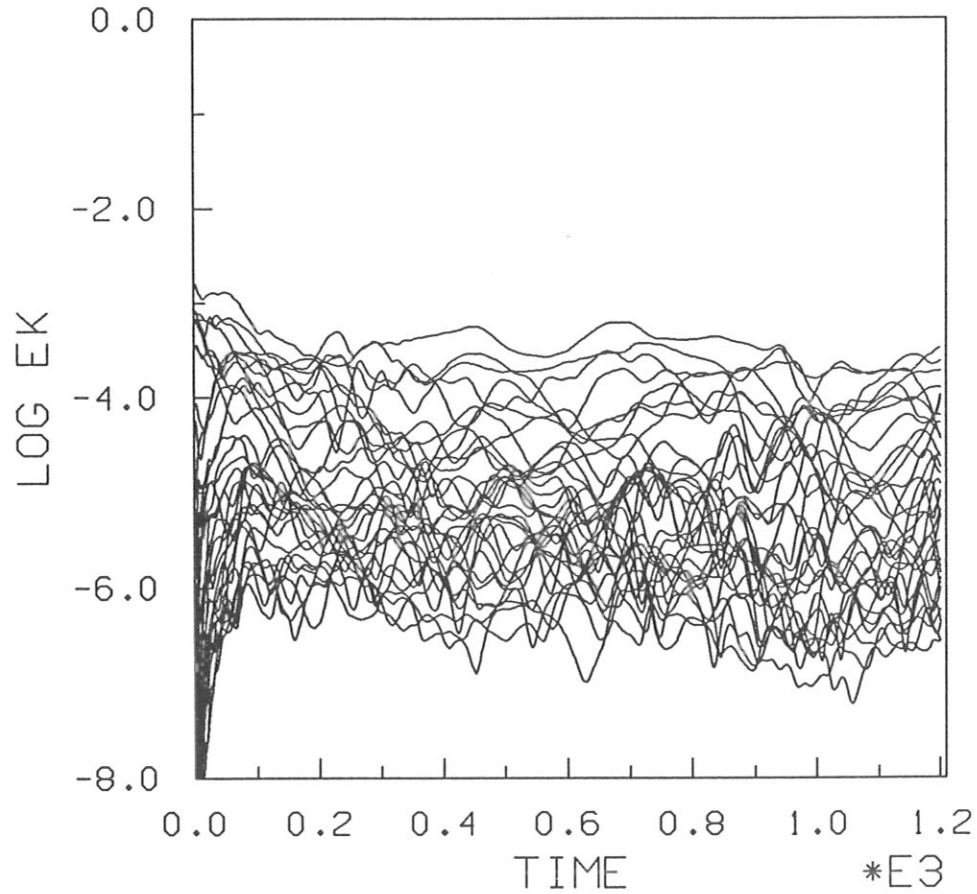


Fig. 17



a)



b)

Fig. 18

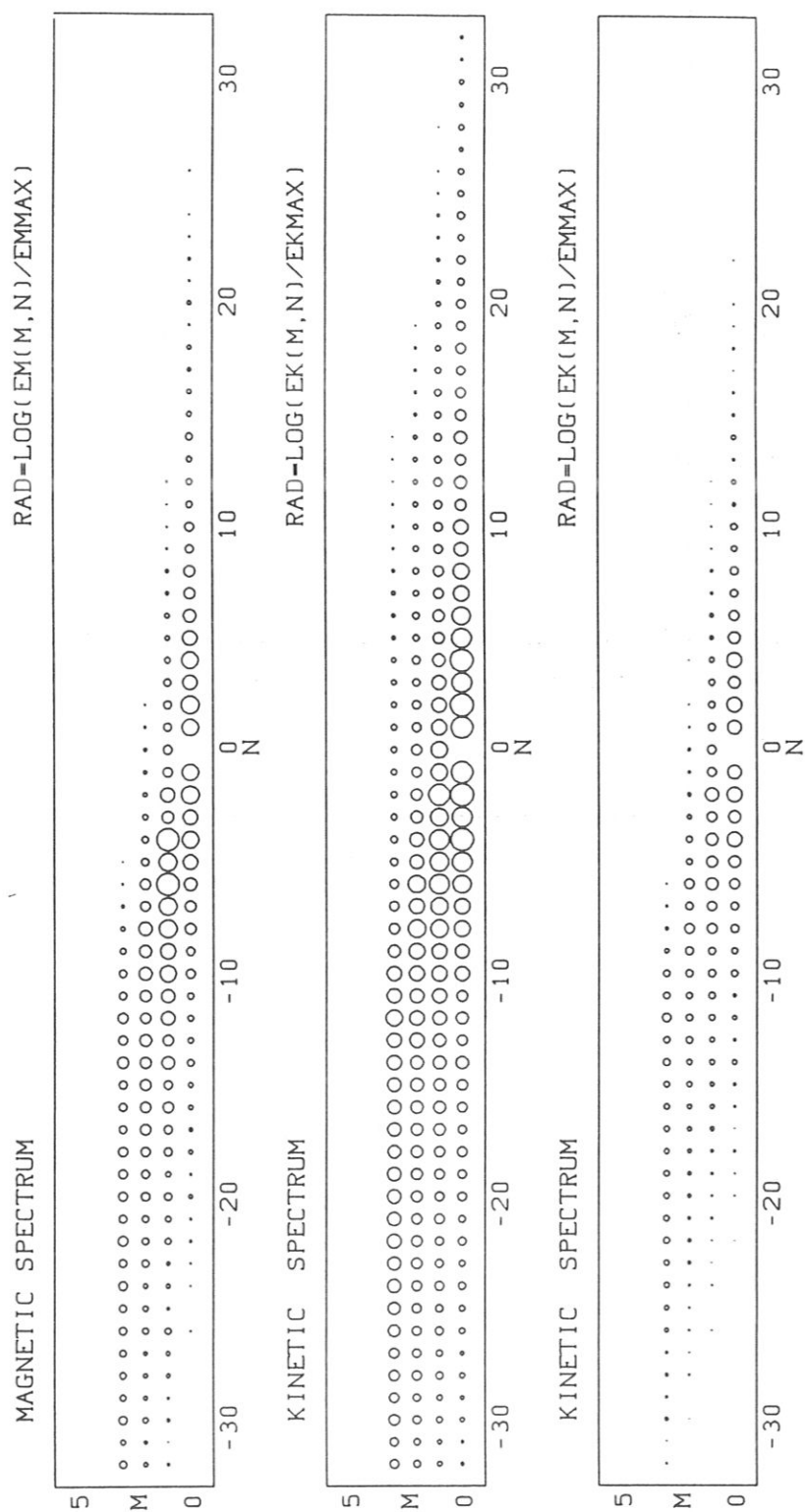


Fig. 19

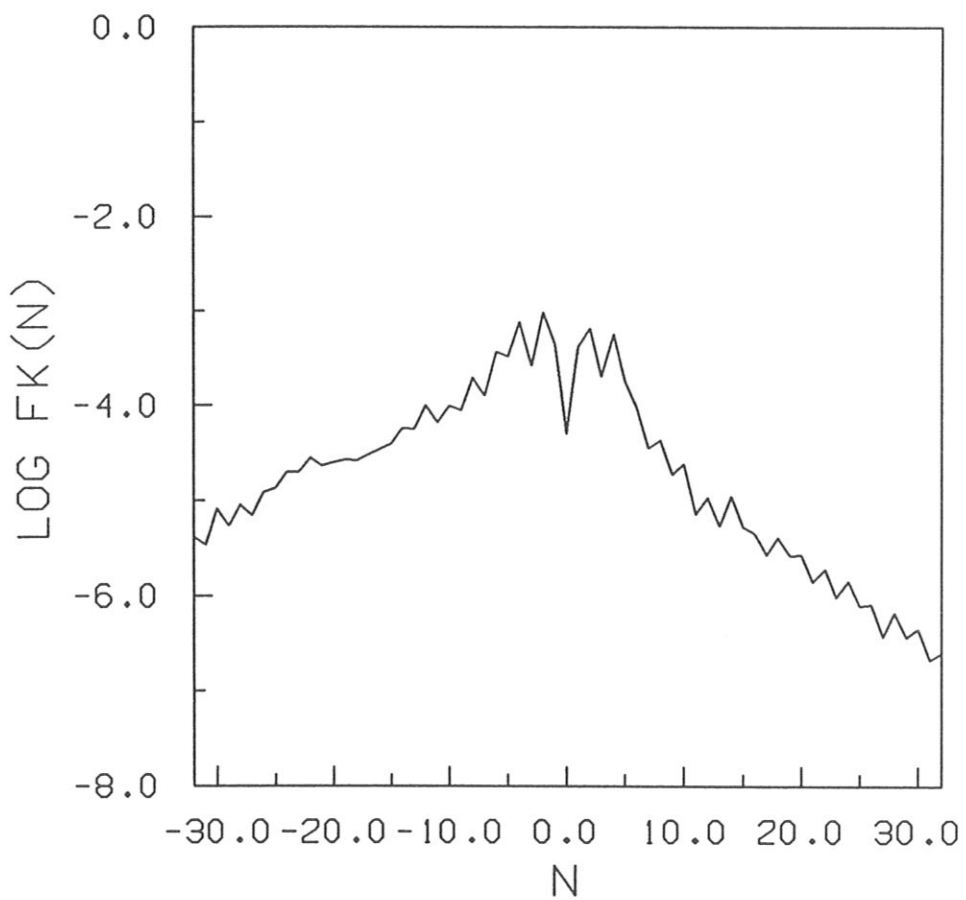
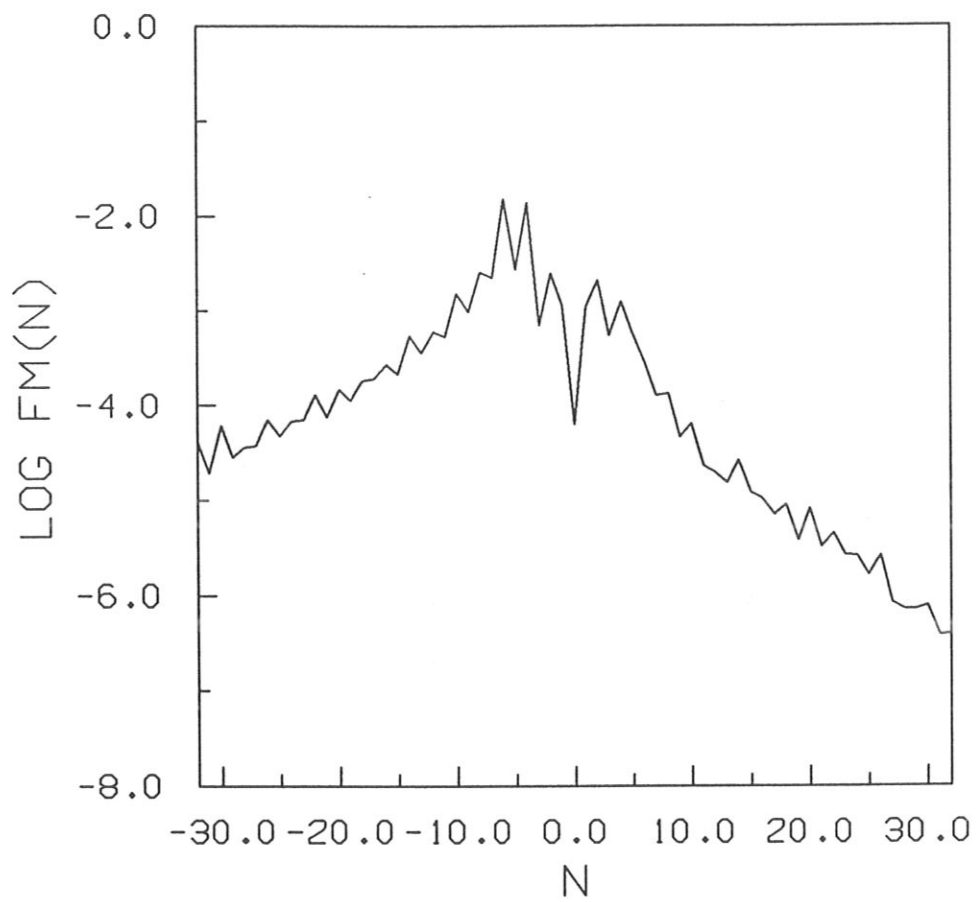


Fig. 20

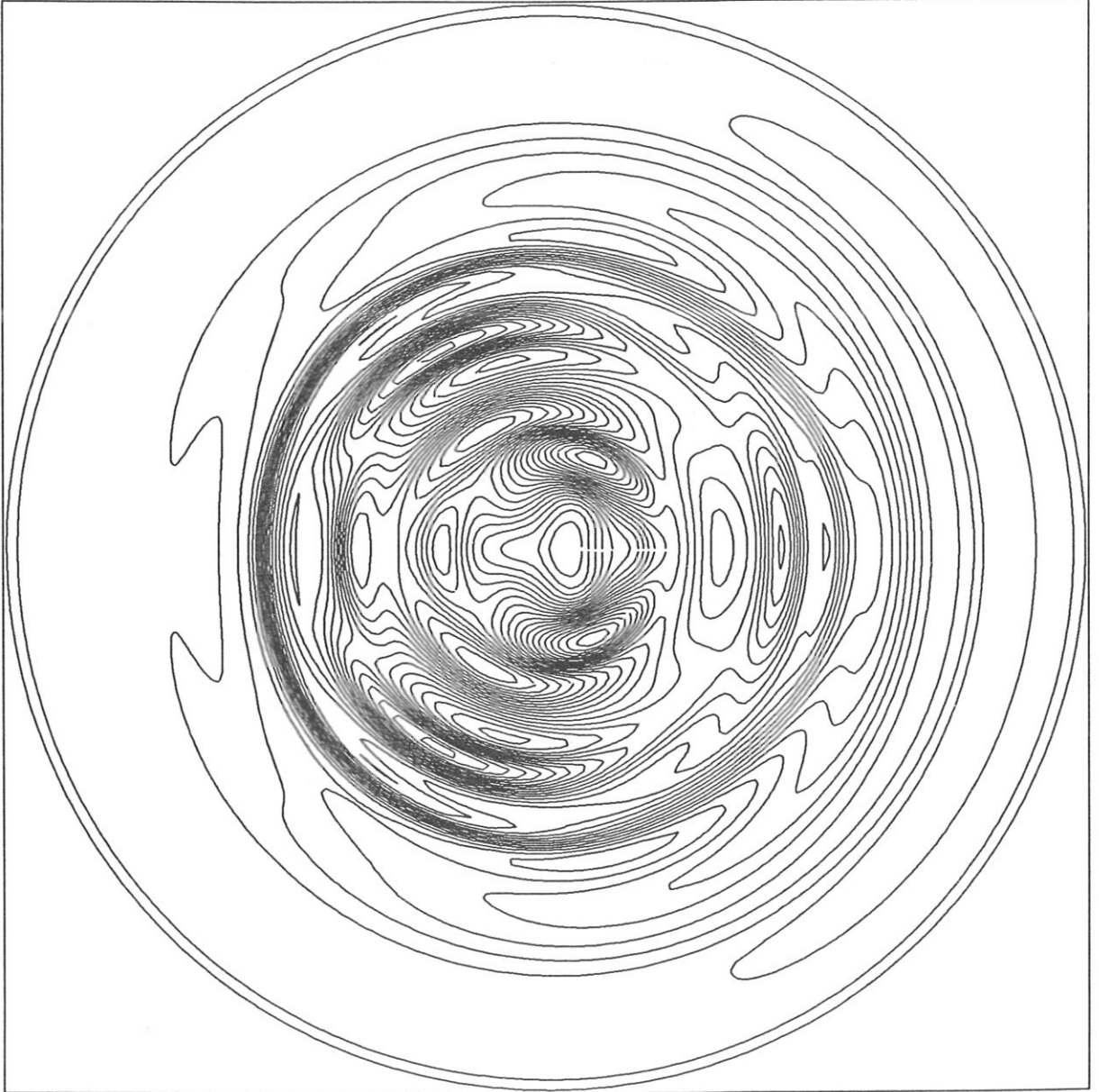


Fig. 21

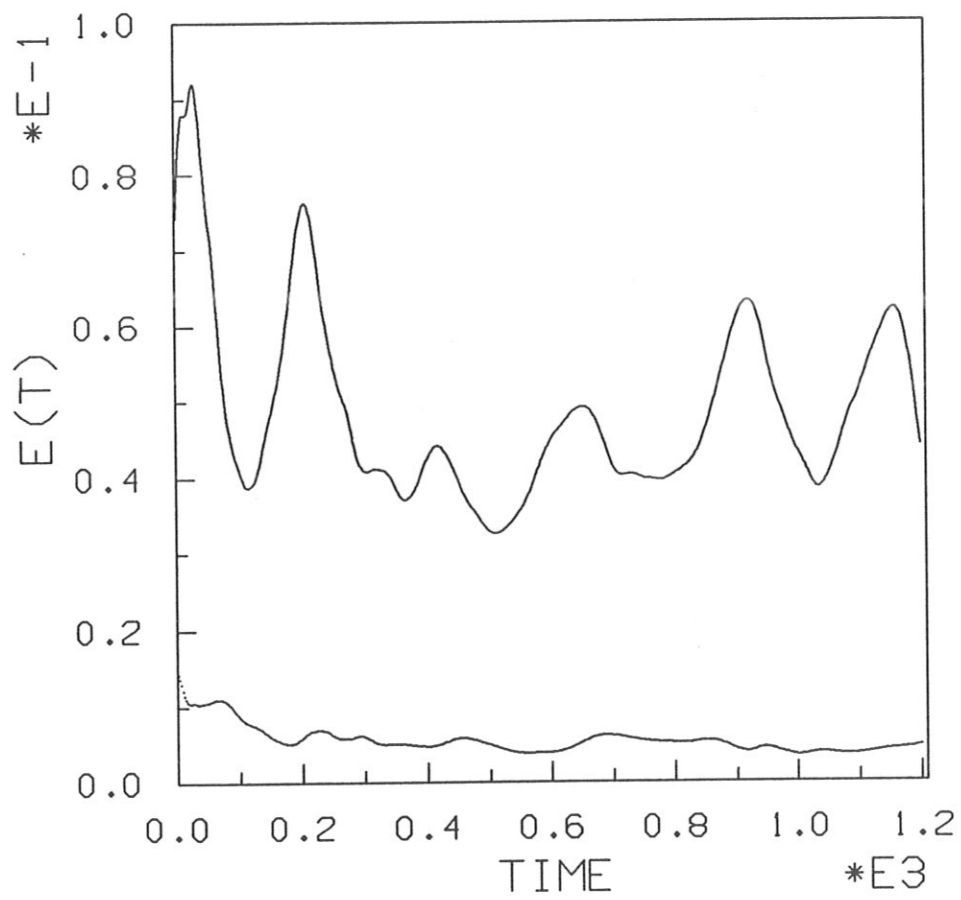


Fig. 22

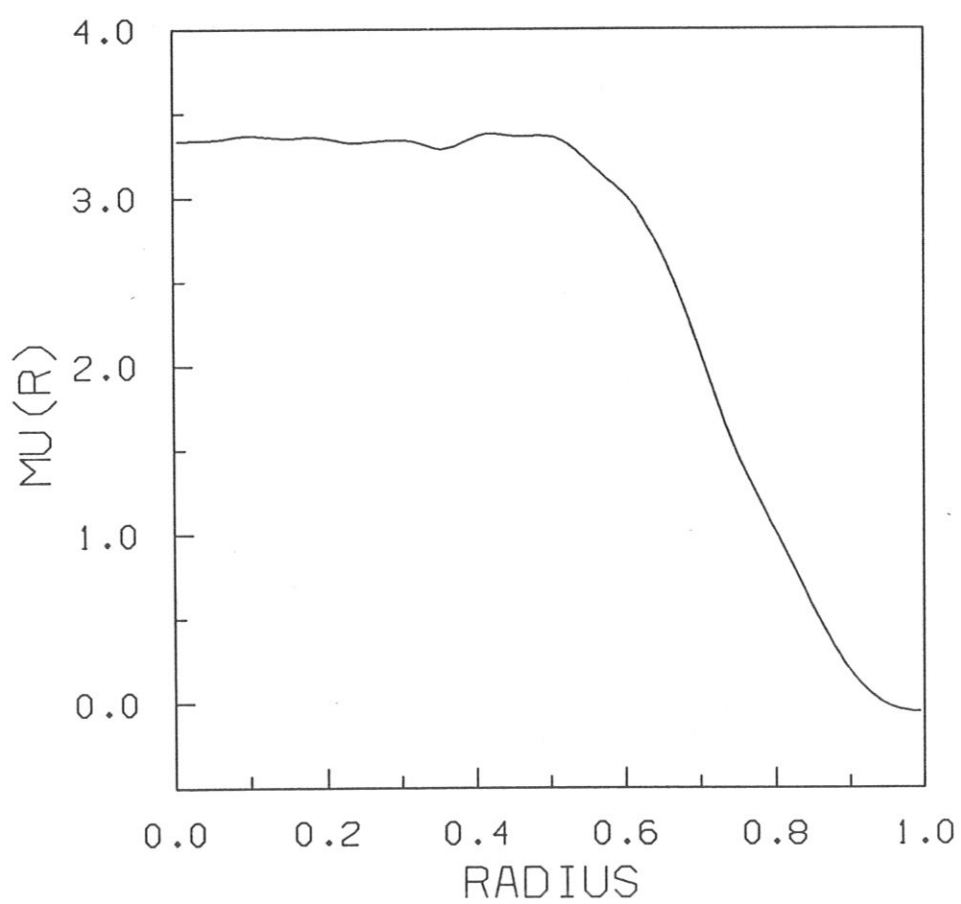
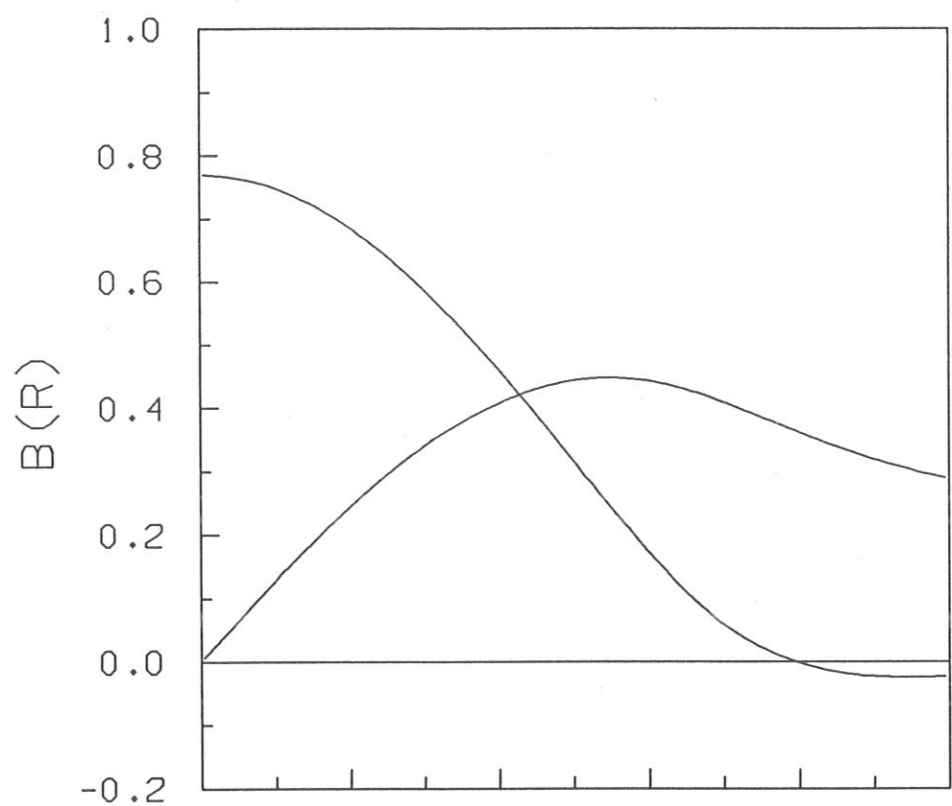
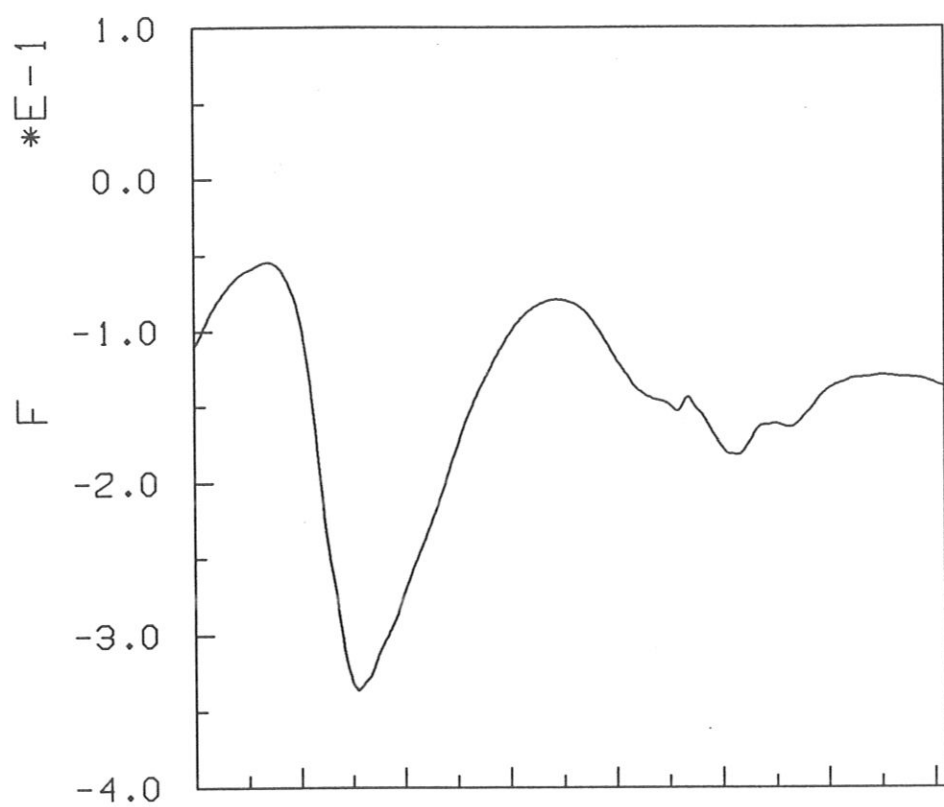
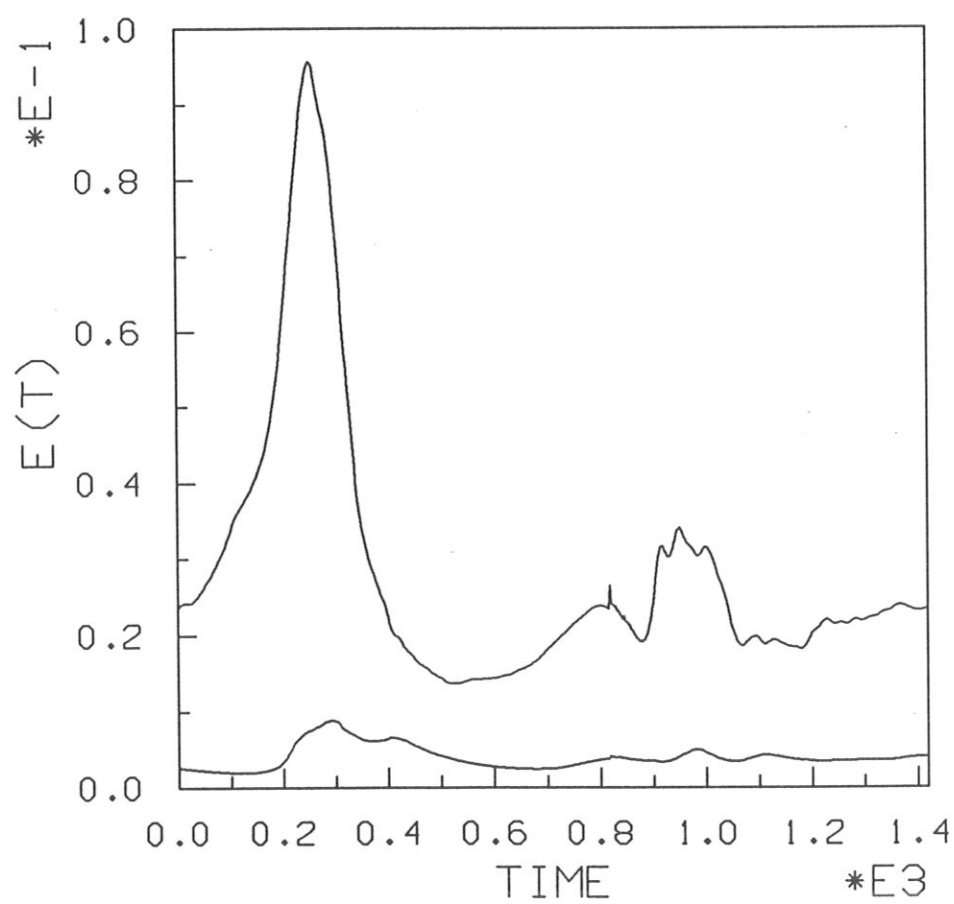


Fig. 23



a)



b)

Fig. 24

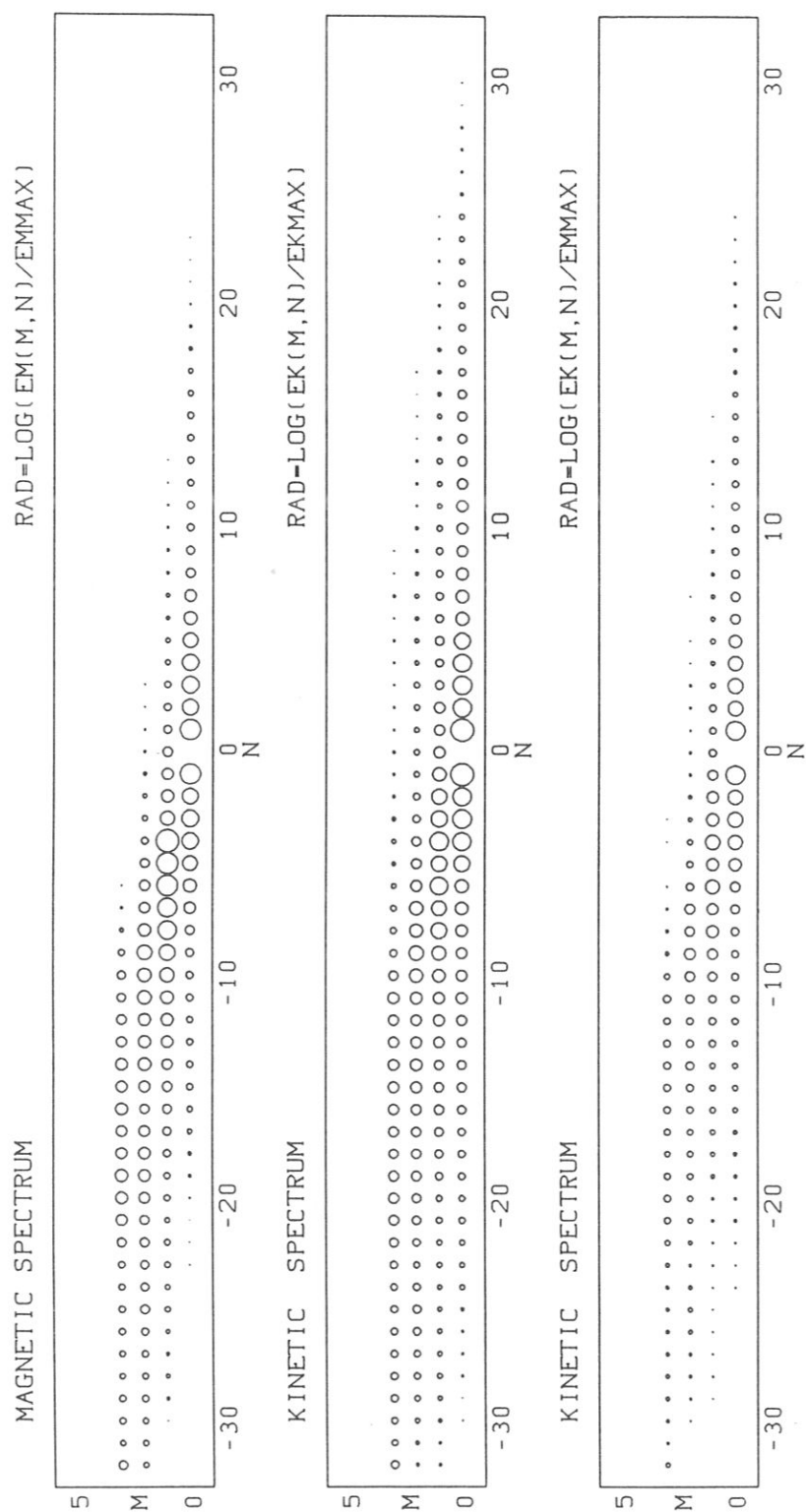


Fig. 25

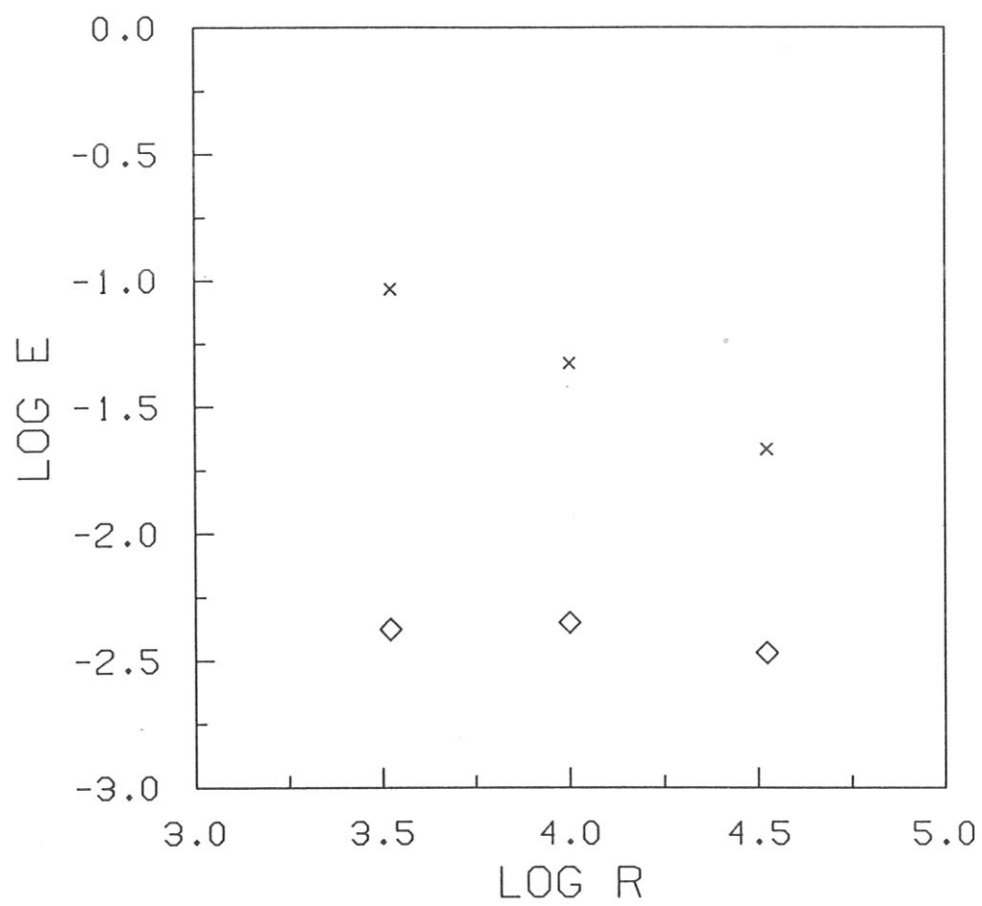


Fig. 26